Enstrophy evolution during head-on wall interaction of premixed flames within turbulent boundary layers

(iD) **Sanjeev Kr. Ghai,** (iD) **Nilanjan Chakraborty,** (iD) **Umair Ahmed, et al.**

COLLECTIONS

Paper published as part of the special topic on Development and Validation of Models for Turbulent Reacting Flows

View Online   Export Citation   CrossMark

ARTICLES YOU MAY BE INTERESTED IN

Modeling subgrid-scale scalar dissipation rate in turbulent premixed flames using gene expression programming and deep artificial neural networks
Physics of Fluids **34**, 085113 (2022); https://doi.org/10.1063/5.0095886

Alignment statistics of pressure Hessian with strain rate tensor and reactive scalar gradient in turbulent premixed flames
Physics of Fluids **34**, 065120 (2022); https://doi.org/10.1063/5.0095389

Assessment of Damköhler's hypotheses in the thin reaction zone regime using multi-step chemistry direct numerical simulations of statistically planar turbulent premixed flames
Physics of Fluids **34**, 055120 (2022); https://doi.org/10.1063/5.0091979

Enstrophy evolution during head-on wall interaction of premixed flames within turbulent boundary layers

View Online   Export Citation   CrossMark

Sanjeev Kr. Ghai,[1] (iD) Nilanjan Chakraborty,[1,a)] (iD) Umair Ahmed,[1] (iD) and Markus Klein[2] (iD)

AFFILIATIONS

[1]School of Engineering, Newcastle University, Newcastle-Upon-Tyne NE1 7RU, United Kingdom
[2]Department of Aerospace Engineering, LRT1, University of the Bundeswehr Munich, Werner-Heisenberg-Weg 39, 85577 Neubiberg, Germany

Note: This paper is part of the special topic, Development and Validation of Models for Turbulent Reacting Flows.
a)Author to whom correspondence should be addressed: Nilanjan.chakraborty@newcastle.ac.uk

ABSTRACT

The statistical behaviors of mean enstrophy and its evolution during head-on interaction of premixed flames propagating toward a chemically inert flat wall across the turbulent boundary layer have been analyzed using direct numerical simulations for a friction velocity-based Reynolds number of $Re_\tau = 110$. The enstrophy dynamics have been analyzed for both isothermal and adiabatic thermal wall boundary conditions. The contributions of vortex-stretching and viscous dissipation are found to be leading order source and sink, respectively, to the mean enstrophy transport in both non-reacting and reacting flows irrespective of the wall boundary condition. However, the contributions due to dilatation rate and baroclinic torque play important roles in addition to the leading order contributions of the vortex-stretching and viscous dissipation terms in the enstrophy transport in turbulent premixed flames. The thermal boundary condition has been demonstrated to affect the near-wall behavior of the enstrophy transport contribution due to dilatation rate, which also affects the near-wall distribution of the enstrophy. The magnitudes of the leading order contributors to the enstrophy transport decrease with the progress of head-on interaction for both wall boundary conditions. Moreover, the overall sink contributions to the enstrophy transport dominate over the source contributions, giving rise to a drop in the mean enstrophy with the progress of head-on interaction. The enstrophy distribution changes significantly during flame-wall interaction, which gives rise to a modification of the relative proportion of the coherent structures in the reacting flow turbulent boundary layer compared to the corresponding non-reacting flow features.

I. INTRODUCTION

The enstrophy statistics play a fundamental role in the analysis of turbulent flow topology[1,2] and also for characterizing the interfaces of turbulent and non-turbulent flow regions.[3–5] An intermittency function was introduced by Libby[4] to distinguish the rotational flow region from the irrotational zones. Dopazo and O'Brien[5] characterized the intermittency function in terms of entrainment velocity which can be expressed in terms of enstrophy. Gorski *et al.*[6] analyzed the statistical behaviors of the different terms of the enstrophy transport equation in turbulent non-reacting channel flows using direct numerical simulations (DNS) data. Bechlars and Sandberg[7] analyzed enstrophy production characteristics and the alignment of vorticity with principal strain rate directions within non-reacting turbulent flat plate boundary layer using DNS data.

In comparison to a vast body of literature for non-reacting flows (e.g., Refs. 1–7 and references therein), relatively limited effort[8–21] has been dedicated to the enstrophy statistics in turbulent premixed flames. It has been found that the self-induced pressure gradient and dilatation rate within a premixed flame due to thermal expansion induced by exothermic chemical reaction can have a significant influence on the evolution of enstrophy[10–16] and the relative alignment of vorticity with local principal strain rates based on DNS data.[8,9,15] Interested readers are referred to a recent review[22] for further information in this regard. Vorticity is known to align preferentially with the intermediate principal strain rate eigendirection in non-reacting turbulent flows[23–30] and non-premixed flames,[31–33] and a qualitatively similar behavior has been reported also for turbulent premixed flames.[8,9,15]

However, the relative alignment of vorticity with the most extensive and most compressive principal strain rate eigenvectors changes with the regime of combustion and the characteristic Lewis number.[9,15] For large Damköhler number values in the corrugated flamelets regime combustion,[9,15] and/or for flames with small sub-unity Lewis number, vorticity has been found to exhibit a considerable collinear alignment with the most compressive strain rate eigendirection, but no collinear alignment has been found with the most extensive principal eigendirection. However, for large values of Karlovitz number (i.e., $Ka \gg 1$), the collinear alignment of vorticity with the most extensive strain rate eigenvector increases in the region of intense heat release despite the predominant vorticity alignment with the intermediate strain rate eigenvector.[9,15] It is not only the alignment of vorticity with the local strain rate eigendirection but also the nature of the evolution of enstrophy from the unburned to the burned gas side is affected by the density ratio σ between unburned and burned gases,[10] body forces,[19] pressure gradient,[19,21] regime of combustion,[12,13,15,16,18,20] and characteristic Lewis number.[11,14,15] The enstrophy magnitude has been found to increase within the flame brush for large values of density ratio σ specifically in the corrugated flamelets regime[10,16] but enstrophy has been found to decay from the unburned to the burned gas side of the flame brush in the thin reaction zones regime (i.e., $Ka > 1$)[12,13,15,16,18,20] for turbulent premixed flames with characteristic Lewis number close to unity (i.e., $Le = 1.0$). However, for flames with $Le < 1$, the enstrophy can increase within the flame even in the thin reaction zones regime.[11,14,15] The presence of body force has been found to alter the pressure gradient within the flame that, in turn, affects the baroclinic torque contribution to the enstrophy evolution in turbulent premixed flames. A recent DNS analysis revealed that baroclinic torque remains negatively correlated with the flame stretch rate in the corrugated flamelets regime flames.[34] In addition to DNS studies, experimental investigations[35,36] utilized stereoscopic particle image velocimetry (PIV) to analyze the enstrophy distribution in turbulent premixed flames. Interested readers are referred to Steinberg *et al.*[36] for a detailed review of the enstrophy statistics for turbulent premixed flames with high turbulence intensities. To date, most analyses on enstrophy statistics in turbulent premixed flames have been conducted in flow configurations which are sufficiently away from the wall. Recently, Lai *et al.*[37] analyzed enstrophy evolutions at different stages of head-on quenching of turbulent premixed flames in a canonical configuration for different values of characteristic Lewis numbers. The effect of a flame propagating toward a wall on the vorticity transport has recently been analyzed by Ohta *et al.*[38] It is reported that the interaction between turbulence and density variation due to combustion can lead to vorticity generation.[38] However, when the flame is sufficiently close to the wall, vortices decay due to the high viscosity of the combusted gas.[38] However, the enstrophy dynamics in turbulent boundary layers during flame-wall interaction (FWI) is yet to be analyzed in detail despite premixed flame-wall interaction taking place in turbulent boundary layers in internal combustion engines, gas turbines and micro-combustors. This gap in the existing literature has been addressed in this paper where enstrophy distribution and its evolution during different stages of head-on interaction of statistically planar flames propagating toward a chemically inert wall across a turbulent boundary layer have been analyzed using DNS data for a friction velocity-based Reynolds number of $Re_\tau = 110$. The enstrophy

dynamics and its evolution in the aforementioned configuration have been analyzed for both isothermal and adiabatic wall boundary conditions in order to isolate the effects of flame quenching due to wall heat loss in the case of head-on interaction with a cold isothermal wall. In this respect, the main objectives of this paper are as follows:

(a) To demonstrate the statistical behaviors of the enstrophy distribution and different terms of its transport equation at different stages of head-on interaction of statistically planar turbulent premixed flames with chemically inert walls in turbulent boundary layers.
(b) To contrast the enstrophy evolution in the case of head-on interaction of turbulent premixed flames in turbulent boundary layers with the corresponding statistics in the case of non-reacting turbulent boundary layer for identical values of friction velocity-based Reynolds number Re_τ.
(c) To study the influence of the thermal boundary condition at the wall on the enstrophy dynamics during head-on interaction of turbulent premixed flames with the wall in turbulent boundary layers.
(d) To provide physical explanations for the observed behaviors in terms of the aspects described above.

The rest of the paper is organized as follows: The mathematical background is provided in Sec. II. This is followed by a brief discussion on the numerical implementation underpinning the current analysis in Sec. III. The results are presented and subsequently discussed in Sec. IV before the main findings are summarized and conclusions are drawn in Sec. V.

II. MATHEMATICAL BACKGROUND

The momentum conservation equation in the ith direction takes the following form:

$$\frac{\partial(\rho u_i)}{\partial t} + \frac{\partial(\rho u_i u_j)}{\partial x_j} = -\frac{\partial p}{\partial x_i} + \frac{\partial \tau_{ij}}{\partial x_j}, \tag{1}$$

where u_i is the ith component of fluid velocity, ρ is the density, p is the pressure, and $\tau_{ij} = \rho\nu(\partial u_i/\partial x_j + \partial u_j/\partial x_i) - (2/3\rho\nu\delta_{ij})(\partial u_k/\partial x_k)$ is the component of the shear stress tensor with ν being the kinematic viscosity. It is possible to derive the transport equation of vorticity $\vec{\omega} = \nabla \times \vec{u}$ upon taking curl of Eq. (1). The transport equation of the ith component of vorticity $\omega_i = \varepsilon_{ijk}\partial u_k/\partial x_j$ [where the symbol ε_{ijk} represents the well-known Levi-Civita symbol usually used for defining the cross product. That is, $\varepsilon_{ijk} = 1$ if (i, j, k) is an even permutation of $(1, 2, 3)$, $\varepsilon_{ijk} = -1$ if it is an odd permutation, and 0 if any index is repeated] takes the following form:[10,11,15,16,19]

$$\frac{\partial \omega_i}{\partial t} + u_k \frac{\partial \omega_i}{\partial x_k} = \underbrace{\omega_k \frac{\partial u_i}{\partial x_k}}_{t_{1i}} \underbrace{-\epsilon_{ijk}\frac{1}{\rho^2}\frac{\partial \rho}{\partial x_j}\frac{\partial \tau_{kl}}{\partial x_l}}_{t_{2i}} + \underbrace{\frac{\epsilon_{ijk}}{\rho}\frac{\partial^2 \tau_{kl}}{\partial x_j \partial x_l}}_{t_{3i}} \underbrace{-\omega_i \frac{\partial u_k}{\partial x_k}}_{t_{4i}}$$

$$+ \underbrace{\frac{\epsilon_{ijk}}{\rho^2}\frac{\partial \rho}{\partial x_j}\frac{\partial p}{\partial x_k}}_{t_{5i}}. \tag{2}$$

The term t_{1i} represents the ith component of the vortex-stretching term, whereas t_{2i} denotes the ith component of the viscous torque term arising from the misalignment between the gradients of viscous

stress and density. The ith component of the third term on the right-hand side (i.e., t_{3i}) is the vorticity diffusion term and becomes identical to $\nu \partial^2 \omega_i / \partial x_j \partial x_j$ in Newtonian fluid flows with constant thermophysical properties. The term t_{4i} represents the destruction of the ith component of vorticity by dilatation rate, whereas the ith component of term $\vec{t_5}$ originates due to the baroclinic torque owing to the misalignment of the density and pressure gradients. The terms $\vec{t_2}$, $\vec{t_4}$, and $\vec{t_5}$ vanish in constant-density low Mach number flows.

By multiplying both sides of Eq. (2) by ω_i, it is possible to obtain the transport equation of enstrophy $\Omega = \frac{\omega_i \omega_i}{2}$,[10,11,15,16,19]

$$\frac{\partial \Omega}{\partial t} + u_k \frac{\partial \Omega}{\partial x_k} = \underbrace{\omega_i \omega_k \frac{\partial u_i}{\partial x_k}}_{T_1} \underbrace{- \epsilon_{ijk} \omega_i \frac{1}{\rho^2} \frac{\partial \rho}{\partial x_j} \frac{\partial \tau_{kl}}{\partial x_l}}_{T_2}$$
$$+ \underbrace{\frac{\epsilon_{ijk} \omega_i}{\rho} \frac{\partial^2 \tau_{kl}}{\partial x_j \partial x_l}}_{T_3} \underbrace{- 2 \frac{\partial u_k}{\partial x_k} \Omega}_{T_4} + \underbrace{\epsilon_{ijk} \frac{\omega_i}{\rho^2} \frac{\partial \rho}{\partial x_j} \frac{\partial p}{\partial x_k}}_{T_5}. \quad (3)$$

Reynolds averaging Eq. (3) yields the Reynolds averaged enstrophy $\overline{\Omega}$,[10,11,15,16,19]

$$\frac{\partial \overline{\Omega}}{\partial t} + \overline{u_k \frac{\partial \Omega}{\partial x_k}} = \underbrace{\overline{\omega_i \omega_k \frac{\partial u_i}{\partial x_k}}}_{T_I} \underbrace{- \overline{\epsilon_{ijk} \omega_i \frac{1}{\rho^2} \frac{\partial \rho}{\partial x_j} \frac{\partial \tau_{kl}}{\partial x_l}}}_{T_{II}}$$
$$+ \underbrace{\overline{\frac{\epsilon_{ijk} \omega_i}{\rho} \frac{\partial^2 \tau_{kl}}{\partial x_j \partial x_l}}}_{T_{III}} \underbrace{- \overline{2 \frac{\partial u_k}{\partial x_k} \Omega}}_{T_{IV}} + \underbrace{\overline{\epsilon_{ijk} \frac{\omega_i}{\rho^2} \frac{\partial \rho}{\partial x_j} \frac{\partial p}{\partial x_k}}}_{T_V}. \quad (4)$$

Here, $\overline{Q}$ indicates the Reynolds averaged value of a general quantity Q. The Favre average of a general quantity Q is given by $\tilde{Q} = \overline{\rho Q}/\overline{\rho}$ and $Q'' = Q - \tilde{Q}$ is the Favre fluctuation of the quantity Q. The dissipation rate $\tilde{\varepsilon}$ of turbulent kinetic energy $\tilde{k} = \overline{\rho u_i'' u_i''}/2\overline{\rho}$ can be expressed as $\overline{\rho}\tilde{\varepsilon} \approx 2\mu\overline{\Omega}$ under isotropic turbulence conditions with the assumption of constant dynamic viscosity μ, and therefore the transport of $\overline{\Omega}$ is important for the purpose of gaining insights into the closure of dissipation rate $\tilde{\varepsilon}$.[39] The term T_I in Eq. (4) is the vortex stretching contribution to the mean enstrophy $\overline{\Omega}$ transport, whereas T_{II} denotes the mean value of the cross-product of two vectors, the density gradient and the viscous torque. The term T_{III} can be expressed as $\overline{\nu \omega_i (\partial^2 \omega_i / \partial x_j \partial x_j)} = \overline{\nu \partial^2 \Omega / \partial x_j^2} - \overline{\nu (\partial \omega_i / \partial x_j)(\partial \omega_i / \partial x_j)}$ for constant dynamic viscosity, and thus T_{III} represents the combined effects of molecular diffusion (i.e., $\overline{\nu \partial^2 \Omega / \partial x_j^2}$) and dissipation [i.e., $-\overline{\nu (\partial \omega_i / \partial x_j)(\partial \omega_i / \partial x_j)}$] of the mean enstrophy $\overline{\Omega}$. The dissipation contribution [i.e., $-\overline{\nu (\partial \omega_i / \partial x_j)(\partial \omega_i / \partial x_j)}$] dominates over the molecular diffusion term (i.e., $\overline{\nu \partial^2 \Omega / \partial x_j^2}$) for high values of turbulent Reynolds number. The term T_{IV} denotes enstrophy dissipation due to dilatation, whereas the baroclinic torque contribution to the enstrophy transport is represented by T_V. The statistical behaviors of $T_I, T_{II}, T_{III}, T_{IV}$, and T_V during head-on interaction of statistically planar flames with chemically inert walls within turbulent boundary layers will be discussed in detail in Sec. IV of this paper.

III. NUMERICAL IMPLEMENTATION

The simulations have been conducted using a three-dimensional fully compressible code called SENGA+,[40] where the conservation equations of mass, momentum, energy, and species are solved in non-dimensional form. In SENGA+, the spatial derivatives are evaluated using a 10th order finite difference central scheme for the internal grid points, whereas the order of accuracy gradually reduces to second order for the non-periodic boundaries. A low storage third order Runge–Kutta scheme[41] has been employed for explicit time advancement. The simulations have been conducted in a configuration where the turbulent boundary layer has formed on top of a chemically inert wall, and for the reacting flow simulations, the initial flow conditions have been generated by a non-reacting fully developed turbulent channel flow solution corresponding to $Re_\tau = \rho_0 u_{\tau,NR} h/\mu_u = 110$, where ρ_0 is the unburned gas density, μ_u is the unburned gas viscosity, and h is the channel half height corresponding to the non-reacting fully developed channel flow solution.

The combustion chemistry for the current analysis is represented by a single-step Arrhenius type chemical reaction (unit mass of Fuel $+ s$ unit mass of Oxidizer $\rightarrow (1+s)$ unit mass of Products, where s is the stoichiometric oxidizer-fuel mass ratio) for the sake of computational economy. A stoichiometric methane-air mixture (i.e., $s = 4.0$) under atmospheric conditions is considered for the current analysis. The fuel reaction rate $\dot{w}_F$ is expressed as $\dot{w}_F = -\rho B^* Y_F Y_O \exp[-\beta(1 - \theta_H)/\{1 - \alpha_H (1 - \theta_H)\}]$, where Y_F and Y_O are the fuel and oxygen mass fractions, respectively. The heat release parameter α_H, the normalized pre-exponential factor B^*, the non-dimensional temperature θ, and the Zel'dovich number β are expressed as $\alpha_H = \tau_H/(\tau_H + 1)$, $\theta_H = (T - T_0)/(T_{ad(\phi=1)} - T_0)$, and $\beta = E_{ac}[T_{ad(\phi=1)} - T_0]/RT_{ad(\phi=1)}^2$ where $\tau_H = (T_{ad(\phi_g=1)} - T_0)/T_0$ is a heat release parameter, T stands for the instantaneous dimensional temperature, T_0 is the unburned gas temperature, $T_{ad(\phi=1)}$ denotes the adiabatic flame temperature for the stoichiometric mixture, and R is the universal gas constant. The activation energy E_{ac} is calculated depending on the equivalence ratio, ϕ, following the methodology proposed by Tarrazo et al.[42] which can capture main flame features (i.e., accurate equivalence ratio ϕ dependence of the unstrained laminar burning velocity $S_{b(\phi)}$ and adiabatic flame temperature $T_{ad(\phi)}$) for hydrocarbon fuels. In the present analysis, the reaction progress variable is defined based on the fuel mass fraction as $c = (Y_{FR} - Y_F)/(Y_{FR} - Y_{FP})$, where subscripts R and P refer to values in the unburned gas and fully burned products, respectively. Accordingly, $\dot{w}_c$ is expressed as: $\dot{w}_c = -\dot{w}_F/(Y_{FR} - Y_{FP})$. For these simulations, all the species are considered to be ideal gases and the thermophysical properties (i.e., dynamic viscosity μ, thermal conductivity λ, specific heats at constant pressure and constant volume c_p and c_v, and density-weighted mass diffusivity ρD) are taken to be temperature independent for the sake of simplicity. Consequently, kinematic viscosity μ/ρ, thermal diffusivity $\lambda/\rho c_p$, and mass diffusivity D increase linearly with temperature. Similar, assumptions have been made in the past in several theoretical and numerical studies.[43–48] The Lewis number of all the species is taken to be unity, and the unburned gas temperature T_0 is taken to be 730 K following previous DNS studies,[49–53] which yields a Zel'dovich number, β, of 6.0, and a heat release rate parameter of $\tau_H = (\sigma - 1) = 2.3$ for the stoichiometric methane–air mixture. Standard constant values are taken for the Prandtl number Pr and the ratio of specific heat, γ (i.e.,

$Pr = 0.7$, $\gamma = c_p/c_v = 1.4$). It has been demonstrated in several previous studies[54,55] that the maximum wall heat flux magnitude and the minimum flame quenching distance can be captured using simple chemistry. Also, the scalar gradient and vorticity statistics obtained from single-step chemistry[54–56] are found to be qualitatively similar to those obtained from detailed chemistry simulation results.[56–58] Moreover, the current analysis focuses on the fluid-dynamical aspects of turbulent flame-wall interaction, and thus the simplification of chemistry is unlikely to affect the conclusions of this analysis.

The computational domain size for the current analysis is considered to be $10.69h \times 1.33h \times 4h$ with an equidistant grid resolution of $1920 \times 240 \times 720$, which ensures at least 8 grid points within the thermal flame thickness $\delta_{th} = (T_{ad} - T_0)/\max|\nabla T|_L$ for $S_L/u_{\tau,NR} = 0.7$ with S_L, $u_{\tau,NR} = \sqrt{|\tau_{w,NR}|/\rho}$ and $\tau_{w,NR}$ being the unstretched laminar burning velocity, friction velocity, and wall shear stress for the non-reacting channel flow, respectively. This grid spacing ensures that the non-dimensional distance to the wall $y^+ = \rho u_\tau y/\mu$ (where y is the distance from the wall) for the wall adjacent grid points is at most $y^+ = 0.6$, and the region $y^+ \leq 1$ has approximately two grid points to ensure appropriate resolution of the viscous sublayer of the turbulent boundary layer. In the channel flow configuration for $Re_\tau = 110$, the longitudinal integral length scale L_{11} and root mean square turbulent velocity u' remain on the order of h and $u_{\tau,NR}$, respectively (Ref. 59), which yields a Damköhler number $Da = L_{11}S_L/u'\delta_{th}$ of 15.80 and a Karlovitz number $Ka = (u'/S_L)^{3/2}(L_{11}/\delta_{th})^{-1/2}$ of 0.36. These values are representative of the corrugated flamelets regime combustion. The key information related to numerical implementation is summarized in Table I, and these values apply to both isothermal and adiabatic boundary conditions.

For these simulations, periodic boundary conditions are imposed for the streamwise (i.e., x-direction) and spanwise (i.e., z-direction), and the mean pressure gradient (i.e., $-\partial p/\partial x = \rho u_{\tau,NR}^2/h$ where p is the pressure) has been imposed in the streamwise flow direction. In the wall-normal direction (i.e., y-direction), a no-slip boundary condition is implemented at $y = 0$, whereas the Dirichlet boundary condition is specified (i.e., $T_w = T_0$) for the isothermal wall boundary condition. By contrast, a Neumann boundary condition, given by $\partial T/\partial y = 0$, is used for the adiabatic wall boundary condition. A partially nonreflecting boundary is specified at $y/h = 1.33$ according to the Navier–Stokes characteristics boundary condition technique proposed by Yoo and Im.[60] This flow configuration is similar to the configuration analyzed earlier by Bruneaux et al.,[61,62] but the variation of density due to temperature change is included in this analysis. In the current simulation setup, the solution from the 1D laminar flame simulation is interpolated to the 3D grid in such a manner that the reaction progress variable $c = 0.5$ is obtained at $y/h \approx 0.85$. The reacting scalar field is initialized in such a manner that the reactant side of the flame faces the wall, whereas the product side of the flame is always facing toward the outflow side of the boundary in the y-direction. The

TABLE I. Key information related to numerical simulations.

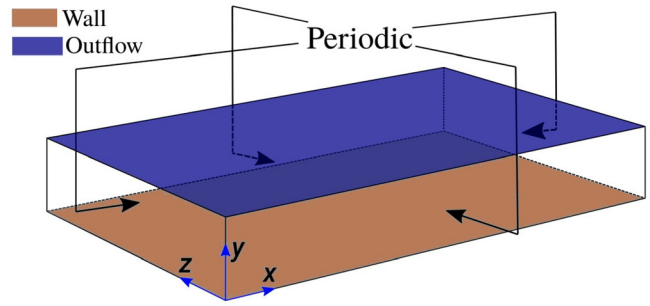| Domain size	Grid size	$Re_\tau = \rho_0 u_{\tau,NR}h/\mu_u$	$S_L/u_{\tau,NR}$
$10.69h \times 1.33h \times 4h$	$1920 \times 240 \times 720$	110.0	0.7

FIG. 1. Schematic diagram of the simulation configuration.

simulation configuration is schematically shown in Fig. 1. The simulations were conducted for 2.0 flow through times based on the maximum axial mean velocity, which is equivalent to $21.30u_{\tau,NR}$. Within the duration of the simulation time, the flame propagates and moves toward the wall and interacts with it, but the turbulent boundary layer does not evolve significantly during the course of the simulation.[53] Interested readers are referred to Refs. 52 and 53 for the validation of the non-reacting channel flow simulation, which are not repeated here for the sake of conciseness.

The Reynolds and Favre averaged quantities involving correlations of Reynolds and Favre fluctuations have been calculated by spatial averaging the quantities of interest in the periodic directions (i.e., $x - z$ planes) for a given time instant.

IV. RESULTS AND DISCUSSION

A. Evolution of the mean enstrophy

The distributions of normalized enstrophy $\Omega \times \nu_u^2/u_{\tau,NR}^4$ (where $\nu_u = \mu_u/\rho_0$ is the unburned gas kinematic viscosity) on the $x - y$ plane at $z/h = 4.0$ at different stages of head-on interaction for both isothermal and adiabatic boundary conditions are shown in Fig. 2 where the contours of $c = 0.1, 0.5$, and 0.9 (from bottom to top) are superimposed on top of the enstrophy field. It can be seen from Fig. 2 that the high magnitudes of enstrophy are confined close to the wall at all time instants during head-on flame-wall interaction. The near wall enstrophy distribution bears the signatures of coherent structures such as ejections and sweeps,[39,63] which, in turn, affect the nature of flame wrinkling as the flame approaches the wall for both isothermal and adiabatic wall boundary conditions. In this configuration, the flame progresses toward the wall with the passage of time, and therefore the simulation domain is progressively occupied by the burned gas with time for both isothermal and adiabatic wall boundary conditions. In the case of isothermal wall, the flame quenches (see, e.g., $t/t_f = 13.12$ and 16.27) in the vicinity of the wall due to heat loss to the wall which has a temperature $T_w = T_0$ and is considerably smaller than the adiabatic flame temperature, whereas in the case of adiabatic boundary condition (i.e., $\partial T/\partial y = 0$ at the wall), the flame extinguishes once all the reactants are consumed. It can be seen from Fig. 2 that the enstrophy magnitude drops significantly in the burned gas, which is consistent with previous findings by Ohta et al.[38] This can further be confirmed from the variation of the normalized Reynolds averaged enstrophy $\overline{\Omega} \times \nu_u^2/u_{\tau,NR}^4$ in the normalized wall normal direction y/h in Fig. 3. The background in Fig. 3 is colored by the local values of the Favre-averaged reaction progress variable $\tilde{c}$.
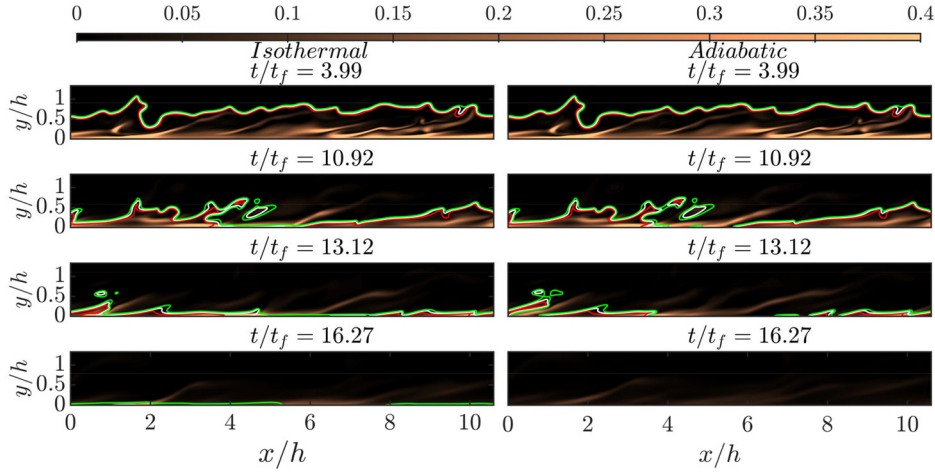
FIG. 2. Distributions of normalized enstrophy $\Omega \times \nu_u^2/u_{\tau,NR}^4$ at the central mid-plane at different stages of head-on interaction along with the contours of $c = 0.1, 0.3, 0.5, 0.7,$ and 0.9 (red, white, and green) for isothermal (left) and adiabatic (right) wall boundary conditions at $t/t_f = 3.99, 10.92, 13.12,$ and 16.27.

Figure 3 shows that the maximum value of $\overline{\Omega} \times \nu_u^2/u_{\tau,NR}^4$ is obtained at the wall (i.e., $y/h = 0$) due to wall-induced velocity gradient and the magnitude of $\overline{\Omega} \times \nu_u^2/u_{\tau,NR}^4$ decreases with increasing y/h. The profile of $\overline{\Omega} \times \nu_u^2/u_{\tau,NR}^4$ with y/h for the non-reacting isothermal flow does not change with time, suggesting that the turbulent boundary layer does not evolve during the flame-wall interaction. The near-wall variations of $\overline{\Omega} \times \nu_u^2/u_{\tau,NR}^4$ for both reacting and non-reacting cases are similar at time $t/t_f = 3.99$ (top row of Fig. 3) when the flame remains away from the wall. However, density and kinematic viscosity change due to the temperature rise across the flame front (i.e., toward large values of y/h) as the flame propagates toward the wall. Hence, the distributions of $\overline{\Omega} \times \nu_u^2/u_{\tau,NR}^4$ for the reacting cases are different to those in the non-reacting cases at advances stages of FWI, e.g., $t/t_f \geq 13.12$. The peak value of $\overline{\Omega} \times \nu_u^2/u_{\tau,NR}^4$ at the wall decreases with time for both isothermal and adiabatic wall boundary conditions, but this drop in $\overline{\Omega} \times \nu_u^2/u_{\tau,NR}^4$ is stronger for the adiabatic wall boundary condition than in the case of the isothermal wall boundary condition (e.g., $t/t_f = 16.27$). In homogeneous isotropic turbulence for non-reacting incompressible flows, the dissipation rate of turbulent kinetic energy $\tilde{\varepsilon}$ can be expressed as $\tilde{\varepsilon} = 2\mu\overline{\Omega}/\overline{\rho}$ (which alternatively suggests $\overline{\Omega} = \overline{\rho}\tilde{\varepsilon}/2\mu$). For turbulent compressible reacting flows, the dissipation rate of turbulent kinetic energy is defined as $\tilde{\varepsilon} = \left[2\overline{\mu s_{ij}'' s_{ij}''} - 2/3\overline{\mu(\partial u_k''/\partial x_k)^2} \right]/\overline{\rho}$ (Ref. 64), where $s_{ij}'' = 0.5(\partial u_i''/\partial x_j + \partial u_j''/\partial x_i)$ is the component of the fluctuating strain rate tensor. The wall-normal variations of $\overline{\rho}\tilde{\varepsilon}/2\mu_u \times \nu_u^2/u_{\tau,NR}^4$ are also compared to $\overline{\Omega} \times \nu_u^2/u_{\tau,NR}^4$ in Fig. 3, which shows that $\overline{\rho}\tilde{\varepsilon}/2\mu_u$ is not identical to $\overline{\Omega}$ in the turbulent boundary layer for both non-reacting and reacting flow conditions. It is shown in the Appendix that the distribution of $\overline{\rho}\tilde{\varepsilon}/2\mu_u \times \nu_u^2/u_{\tau,NR}^4$ for the non-reacting flow case considered here remains in good quantitative agreement with previous DNS findings[6] at $Re_\tau = 145$, and this distribution is also in good qualitative agreement with previous experimental data[65] at $Re_\tau = 890$. Figure 3 shows that the $\overline{\Omega}$ distribution is qualitatively similar to $\overline{\rho}\tilde{\varepsilon}/2\mu_u$ for $y/h > 0.25$, and there is also a significant amount of quantitative agreement between $\overline{\Omega}$ and $\overline{\rho}\tilde{\varepsilon}/2\mu_u$ in the order

of magnitude sense in the non-reacting flow considered here although the fluid flow is neither homogeneous nor isotropic in nature. However, the distributions of $\overline{\Omega}$ and $\overline{\rho}\tilde{\varepsilon}/2\mu_u$ are both qualitatively and quantitatively different in the reactive cases irrespective of the wall boundary condition, and therefore $\overline{\rho}\tilde{\varepsilon} \approx 2\mu\overline{\Omega}$ cannot be used for flame-wall interaction within turbulent boundary layers.

B. Evolutions of the terms of the mean enstrophy transport equation

In order to explain the decay of $\overline{\Omega}$ with time and the distribution of $\overline{\Omega}$ in the wall normal direction, the variations of the source/sink terms of the enstrophy transport equation (i.e., $T_I, T_{II}, T_{III}, T_{IV},$ and T_V) in the wall-normal distance are shown in Fig. 4. It can be seen from Fig. 4 that in the non-reacting isothermal case, the vortex stretching term T_I and the combined diffusion and dissipation term T_{III} remain the leading order source and sink, respectively, in the enstrophy transport and they remain in approximate equilibrium. The magnitudes of the terms arising from the misalignment between density gradient and viscous stress gradient T_{II}, dilatation rate T_{IV} and baroclinic torque T_V remain negligible in comparison to those of T_I and T_{III}. The magnitudes of positive and negative values of T_I and T_{III} decrease with wall normal distance, and their maximum values are obtained close to the wall (at around $y/h = 0.05$) for the non-reacting isothermal flow. The same qualitative behavior is observed at early time instants (e.g., $t/t_f = 3.99$) in the case of head-on flame-wall interaction for both isothermal and adiabatic boundary conditions. The leading order source and sink contributions of T_I and T_{III}, respectively, in the non-reacting channel flow are consistent with previous findings.[6]

The flame starts to interact with the wall at $t/t_f > 10$, and the magnitudes of the leading order contributors to the enstrophy transport decrease with the progress of flame-wall interaction. The vortex-stretching term T_I acts as a leading order source term to the enstrophy transport for the reactive cases irrespective of the wall boundary condition but its magnitude drops with the progress of head-on interaction (i.e., with the passage in time). The magnitude of the term due to mismatch between the density gradient and viscous stress gradient T_{II} remains small in comparison to the leading order contributions of T_I
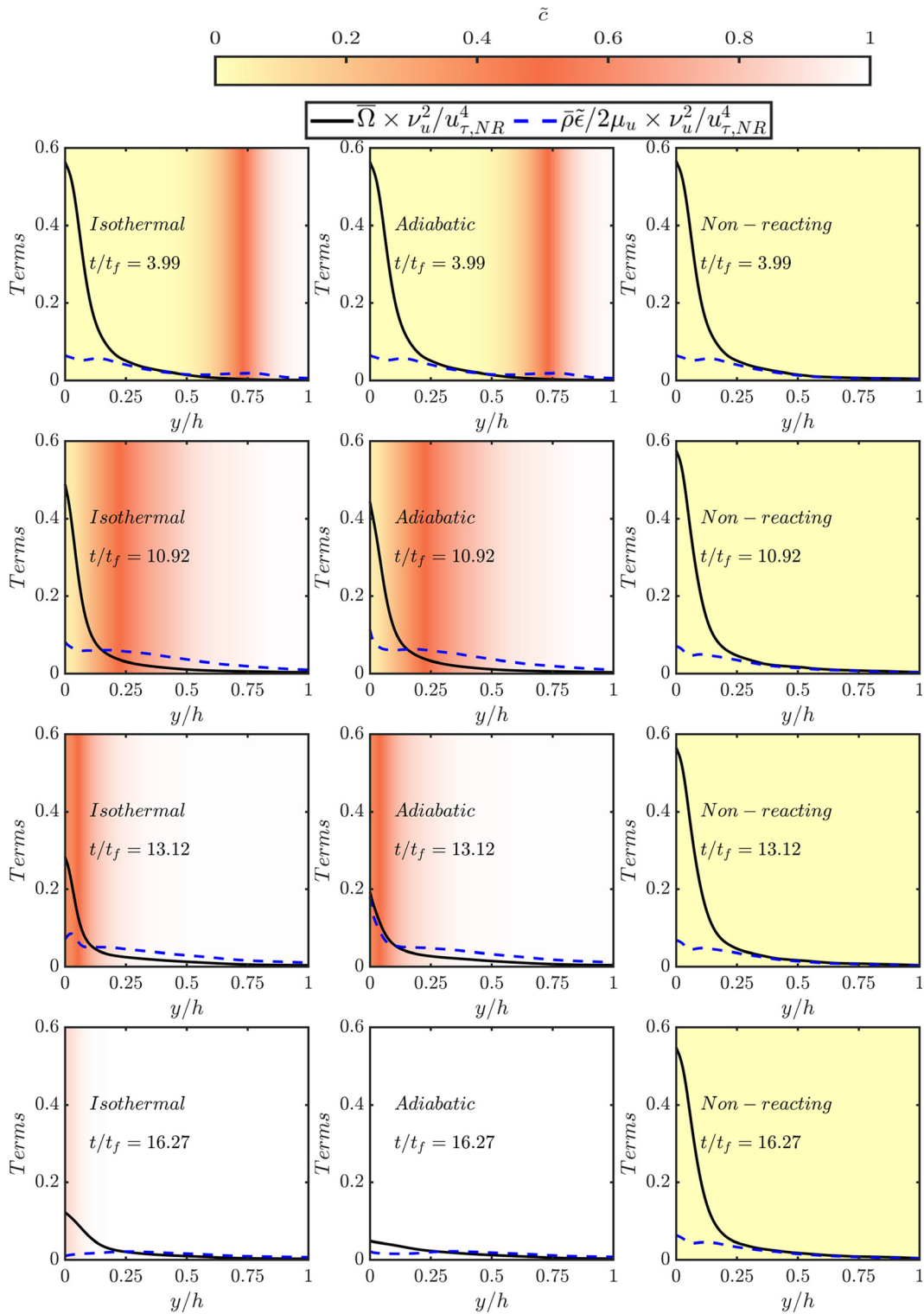
FIG. 3. Variations of the normalized Reynolds averaged enstrophy $\overline{\Omega} \times \nu_u^2/u_{\tau,NR}^4$ and normalized dissipation rate of turbulent kinetic energy $\overline{\rho\tilde{\epsilon}}/2\mu_u \times \nu_u^2/u_{\tau,NR}^4$ with the normalized wall normal distance y/h for isothermal (left) and adiabatic (right) wall boundary conditions at $t/t_f = 3.99$, 10.92, 13.12, and 16.27 (top to bottom). The background color in Figs. 3–11 and 13–19 shows the local values of $\tilde{c}$.
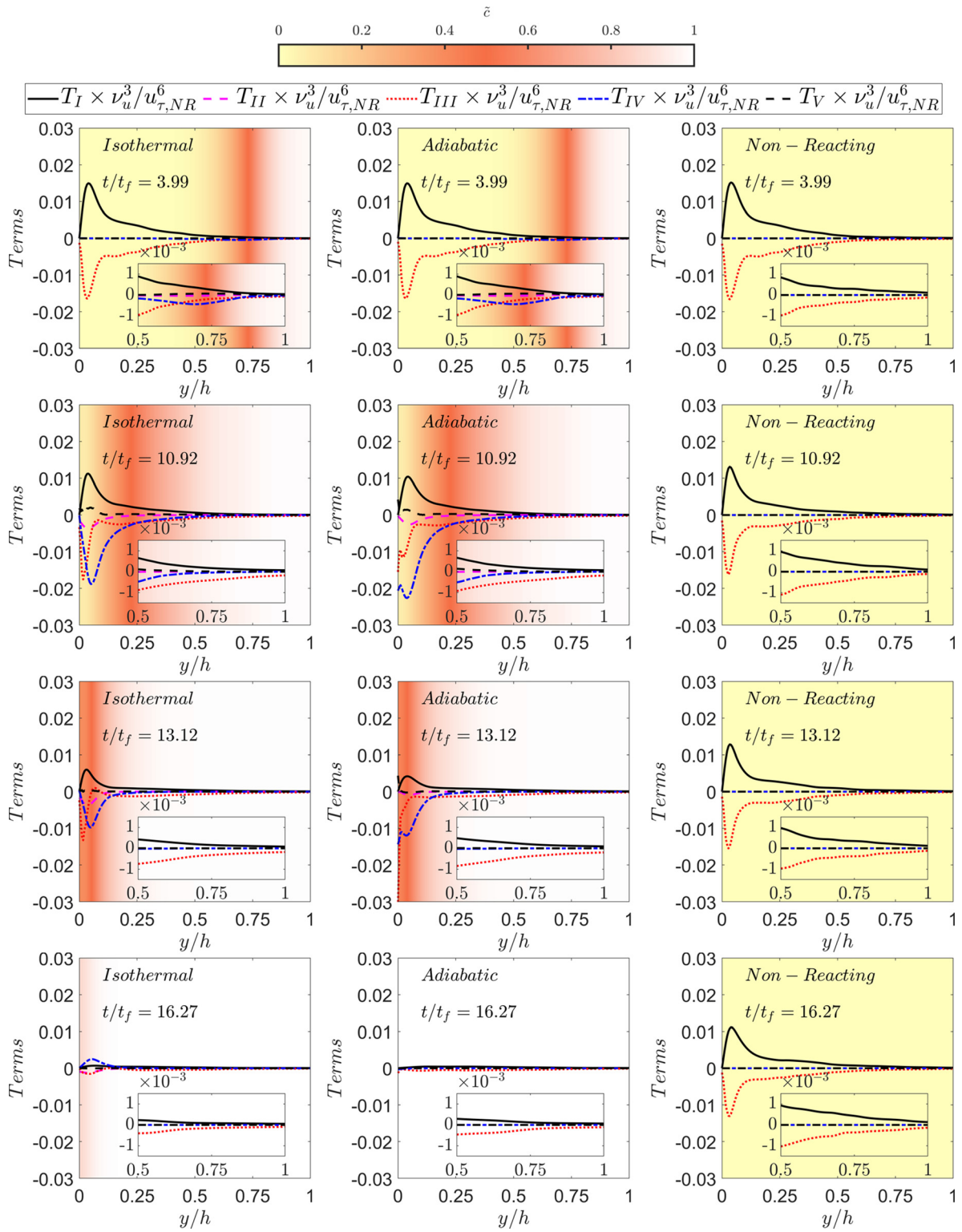
FIG. 4. Variations of the normalized source/sink terms of the enstrophy transport equation (i.e., $\{T_I, T_{II}, T_{III}, T_{IV}, \text{ and } T_V\} \times \nu_u^3/u_{\tau,NR}^6$) with the normalized wall normal distance y/h for isothermal (left) and adiabatic (right) wall boundary conditions at $t/t_f = 3.99$, 10.92, 13.12, and 16.27 (top to bottom).

and T_{III} when the flame is away from the wall and during early stages of flame-wall interaction (e.g., $t/t_f = 10.92$), but the magnitude of this term becomes comparable to that of T_{III} at the final stages of flame-wall interaction (e.g., $t/t_f = 13.12$ and 16.27) in the case of isothermal wall boundary condition; however, the magnitude of this term remains negligible at all stages of flame-wall interaction in the case of adiabatic wall boundary condition. At the early stages of flame-wall interaction (e.g., $t/t_f = 10.92$), the term due to dilatation rate contribution T_{IV} becomes a major sink alongside the combined viscous diffusion and dissipation term T_{II}. However, at the final stage of flame quenching (e.g., $t/t_f = 16.27$), the dilatation rate contribution T_{IV} assumes positive values in the case of isothermal wall boundary condition, whereas T_{IV} assumes small but still negative values in the case of adiabatic wall boundary condition. The baroclinic torque contribution T_V assumes significant values only within the flame brush. The term T_V assumes positive values with magnitudes comparable to T_{IV} when the flame remains away from the wall (e.g., $t/t_f = 3.99$), and the magnitude of its positive contribution close to the wall starts to increase with the progress of head-on interactions (compare $t/t_f = 10.92$ and 13.12). The behaviors of the source/sink terms of the enstrophy transport equation (i.e., $T_I, T_{II}, T_{III}, T_{IV}$, and T_V) are found to be consistent with previous findings in the case of premixed flames[10,11,13,14,17] and also in the case of conventional head-on quenching configurations.[33] It is also shown in the Appendix that the components of T_I and T_{III} for the non-reacting flow, which are available from previous DNS findings[6] at $Re_\tau = 145$, are in good agreement, and they are also in good qualitative agreement with previous experimental data[54] at $Re_\tau = 890$.

A comparison of the magnitudes of $T_I, T_{II}, T_{III}, T_{IV}$, and T_V in Fig. 4 indicates that the magnitudes of the combined contributions of the sink terms dominate over the combined magnitudes of the source terms in the reactive cases during head-on interaction irrespective of the wall boundary condition, which leads to a drop in the enstrophy magnitude with the progress of flame-wall interaction with time.

The dilatation contribution T_{IV} starts to act as a source term in the isothermal wall case at the later stages of head-on interaction (e.g., $t/t_f = 16.27$) (see Fig. 4), whereas this term continues to be a sink in the case of adiabatic wall. Therefore, the decay in the enstrophy magnitude is more rapid in the adiabatic wall case than in the isothermal wall case (see Fig. 3).

In order to explain the differences between the enstrophy evolutions for different thermal boundary conditions, it is worthwhile to present the temporal evolutions of the wall-normal variations of Reynolds averaged values of normalized mean density $\overline{\rho}/\rho_0$, Favre-averaged non-dimensional temperature $\tilde{\theta} = (\tilde{T} - T_0)/(T_{ad} - T_0)$, and Reynolds averaged reaction rate of reaction progress variable $\overline{\dot{w}_c} \times \delta_{th}/\rho_0 S_L$, which are shown in Fig. 5 at different time instants. Figure 5 shows that the equality between $\tilde{c}$ and $\tilde{\theta}$ holds when the flame remains away from the wall (e.g., $t/t_f = 3.99$) as expected for low Mach number unity Lewis number conditions, but the equality between $\tilde{c}$ and $\tilde{\theta}$ is lost during flame-wall interaction in the case of the isothermal boundary condition, while $\tilde{c} = \tilde{\theta}$ is maintained at all stages in the case of the adiabatic boundary condition. In the case of the isothermal boundary condition, $\tilde{\theta}$ remains 0.0 at the wall but $\tilde{c}$ at the wall continues to increase during flame-wall interaction even after flame quenching (i.e., even after $\overline{\dot{w}_c}$ disappears) because of the diffusion of unburned reactants from the wall to the interior of the domain. It can further be seen from Fig. 5 that $\overline{\dot{w}_c}$ vanishes in the isothermal case due to heat loss through the wall once the flame is in proximity to the wall. Moreover, $\overline{\dot{w}_c}$ remains vanishingly small at the wall at all stages in the isothermal case but $\overline{\dot{w}_c}$ assumes non-zero values at the wall during head-on interaction in the adiabatic case which is also accompanied by the increases in $\tilde{c}$ and $\tilde{\theta}$ until the fuel is fully consumed. The gas density drops with an increase in $\tilde{\theta}$ and therefore $\overline{\rho} \approx \rho_0$ is maintained at the wall in the isothermal case, whereas $\overline{\rho}$ decreases at the wall and remains smaller than ρ_0 with the progress of head-on interaction in the case of the adiabatic wall. The density ρ appears explicitly
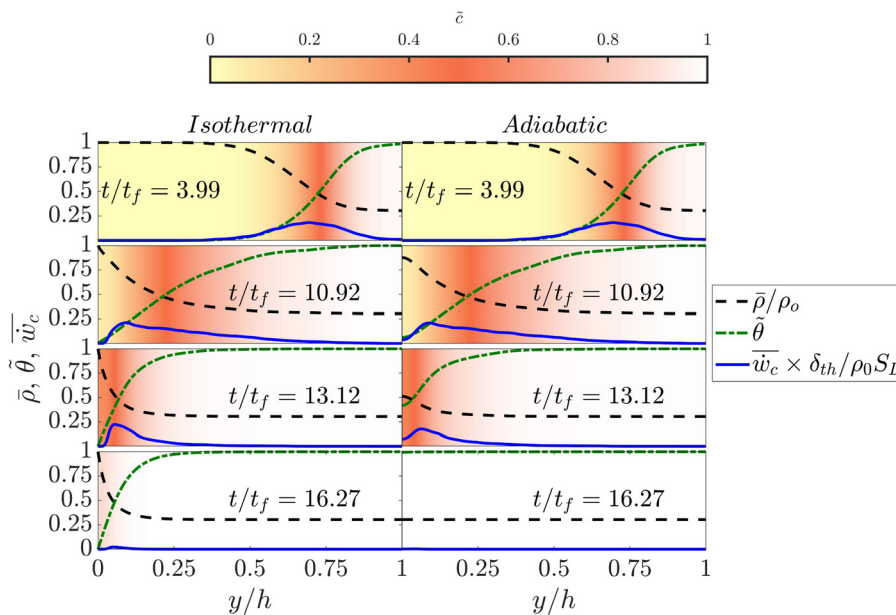

FIG. 5. Variations of normalized mean density $\overline{\rho}/\rho_0$, Favre-averaged non-dimensional temperature $\tilde{\theta} = (\tilde{T} - T_0)/(T_{ad} - T_0)$ and Reynolds averaged reaction rate of reaction progress variable $\tilde{\dot{w}}_c \times \delta_{th}/\rho_0 S_L$ with the normalized wall normal distance y/h for isothermal (left) and adiabatic (right) wall boundary conditions at $t/t_f = 3.99$, 10.92, 13.12, and 16.27 (top to bottom).

in the enstrophy transport equation [see Eqs. (3) and (4)], and it is coupled to temperature via the ideal gas law. Moreover, for a reacting flow, temperature is also closely linked to the reaction progress variable. Due to the different temperature boundary conditions, there is a direct impact on the variation of density in the vicinity of the wall, and this can be clearly seen in Fig. 5 at advanced stages of FWI.

The gas density ρ can be expressed as $\rho = \rho_0/(1 + \tau\theta)$, which leads to $\nabla\rho = -\tau\rho^2\nabla\theta/\rho_0$ and $\partial u_i/\partial x_i = \tau\rho S_\theta|\nabla\theta|/\rho_0$, where $S_\theta = (D\theta/Dt)/|\nabla\theta|$ is the displacement speed of temperature isosurfaces. The wall-normal distributions of $\overline{|\nabla c|} \times \delta_{th}$, $\overline{|\nabla\theta|} \times \delta_{th}$, $\overline{|\nabla\rho|} \times \delta_{th}/\rho_0$, and $\overline{\partial u_i/\partial x_i} \times \delta_{th}/S_L = \overline{\tau\rho S_\theta|\nabla\theta|}/\rho_0 \times \delta_{th}/S_L$ at different time instants are shown for both wall boundary conditions in Fig. 6. The temporal evolution of the mean normalized wall heat flux magnitude $\overline{\Phi}_w = q_w/[\rho_0 c_{p0} u_{\tau,NR}(T_{ad} - T_0)]$ (where q_w is the wall heat flux magnitude and c_{p0} is the specific heat at constant pressure in the unburned gas) in the isothermal wall case is shown in Fig. 7. It can be seen from Fig. 6 that $\overline{|\nabla c|} \approx \overline{|\nabla\theta|}$ is maintained when the flame is away from the wall in the isothermal wall boundary condition when the mean normalized wall heat flux magnitude $\overline{\Phi}_w$ remains negligible, but this equality is lost when $\overline{\Phi}_w$ takes significant values indicating heat loss through the wall, which prompts a reduction of $\overline{w}_c$ in the near-wall region as a result of flame quenching (see Fig. 5). This is also consistent with the loss of equality between $\tilde{c}$ and $\tilde{\theta}$ during head-on interaction in the case of isothermal wall (see Fig. 5). For the
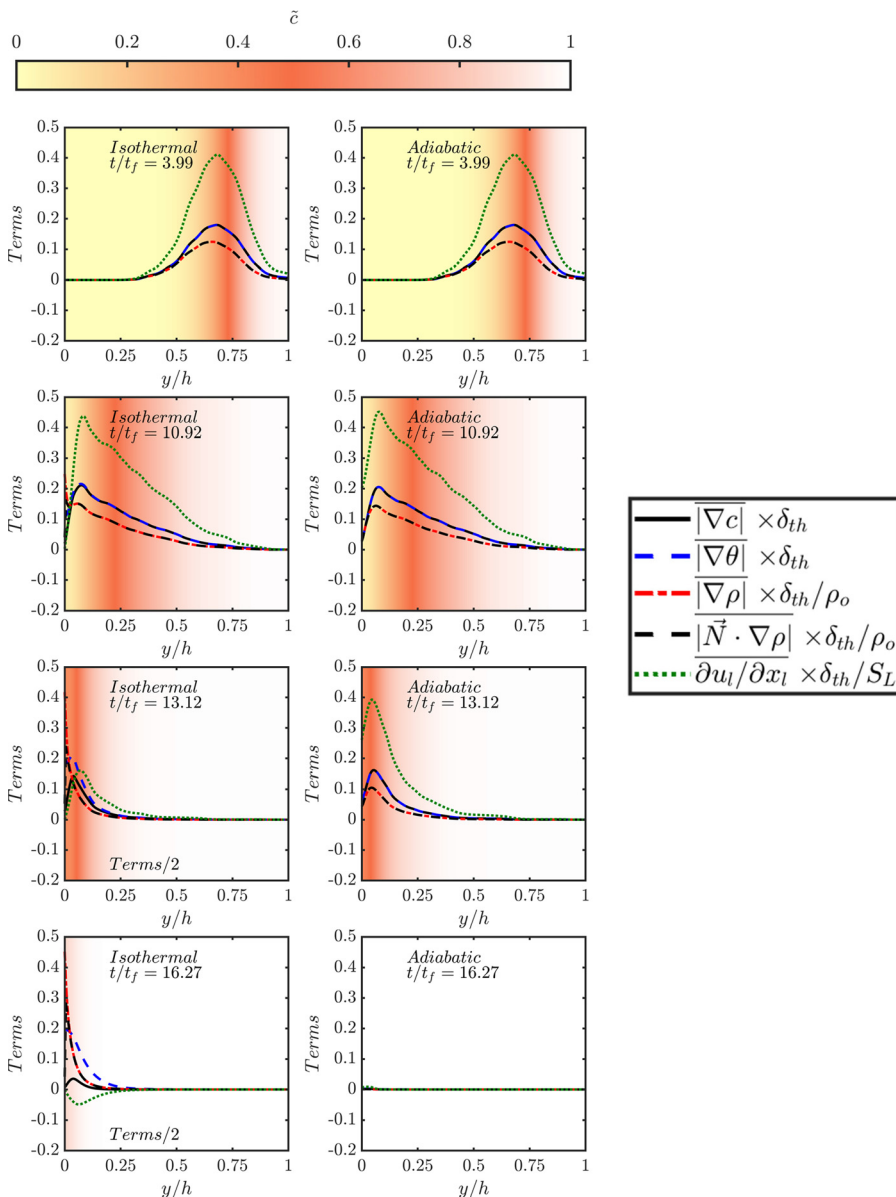

FIG. 6. Variations of $\overline{|\nabla c|} \times \delta_{th}$, $\overline{|\nabla\theta|} \times \delta_{th}$, $\overline{|\nabla\rho|} \times \delta_{th}/\rho_0$, $\overline{|\vec{N}\cdot\nabla\rho|} \times \delta_{th}/\rho_0$ and $\overline{\partial u_i/\partial x_i} \times \delta_{th}/S_L$ with the normalized wall normal distance y/h for isothermal (left) and adiabatic (right) wall boundary conditions at $t/t_f = 3.99$, 10.92, 13.12, and 16.27 (top to bottom).
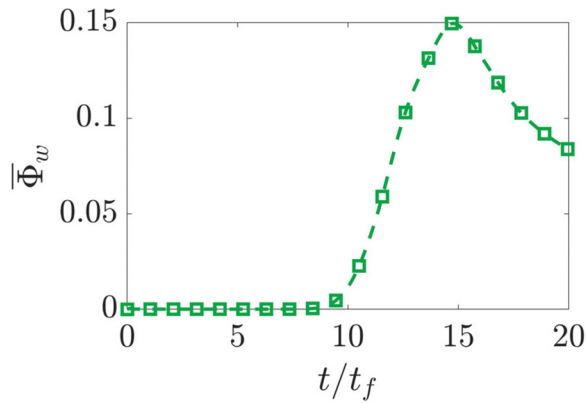
FIG. 7. Temporal evolution of the mean normalized wall heat flux magnitude $\overline{\Phi}_w = q_w/[\rho_0 c_{p0} u_{\tau,NR}(T_{ad} - T_0)]$ for the isothermal wall boundary condition.

isothermal wall case, $\overline{|\nabla\theta|}$ assumes greater values than $\overline{|\nabla c|}$ close to the wall due to high temperature gradient at the wall because of flame quenching (note the quenching distance δ_Q is about $0.8\delta_{th}$ in this case), whereas the wall-normal component of ∇c vanishes due to impenetrability, which leads to $\overline{|\nabla\theta|} > \overline{|\nabla c|}$ in the isothermal wall boundary condition. In contrast, wall normal components of $\nabla\theta$ and ∇c vanish at the wall in the case of adiabatic wall boundary condition, which gives rise to comparable values of $\overline{|\nabla\theta|}$ and $\overline{|\nabla c|}$ at the wall. It can further be seen from Fig. 6 that $\overline{|\nabla c|}$ drops at the wall during the head-on interaction for both wall boundary conditions. However, the peak values of $|\nabla\theta|$ and $|\nabla c|$ at the advanced stages of head-on interaction (e.g., $t/t_f = 16.27$) remain greater in the case of isothermal wall boundary condition than in the case of an adiabatic wall. The flame quenching in the case of isothermal wall leads to steeper gradients of c and θ close to the wall than those in the case of adiabatic wall boundary condition. The physical mechanisms responsible for the reduction in $|\nabla c|$ at the wall in both isothermal and adiabatic boundary conditions are explained elsewhere,[52] which are not repeated here.

Figure 6 shows that the wall normal variation of $\overline{|\nabla\rho|} \times \delta_{th}/\rho_0$ is qualitatively similar to that of $\overline{|\nabla\theta|} \times \delta_{th}$, which is consistent with $\nabla\rho = -\tau\rho^2\nabla\theta/\rho_0$. This also sets up higher values of $\overline{|\nabla\rho|}$ close to the wall in the case of isothermal boundary condition than in the adiabatic boundary condition due to steeper thermal gradient at the wall in the isothermal case. Greater magnitudes of $\nabla\rho$ in the isothermal case are responsible for higher magnitude of T_{II} in this case at the final stages of flame-wall interaction (e.g., $t/t_f = 16.27$) than in the case of an adiabatic wall. In the case of adiabatic wall, $\overline{|\nabla\theta|}$ remains small close to the wall at all stages of flame-wall interaction and in the case of adiabatic wall, $\dot{\overline{w}}_c$ does not vanish at the wall and the flame extinguishes only when all the reactants are consumed. This implies that $S_\theta = (D\theta/Dt)/|\nabla\theta|$ remains predominantly positive in the case of an adiabatic wall, which leads to predominantly positive values of $\partial u_i/\partial x_i = \tau\rho S_\theta|\nabla\theta|/\rho_0$. This can be substantiated from positive values of $\overline{\partial u_i/\partial x_i} = \overline{\tau\rho S_\theta|\nabla\theta|}/\rho_0$ (see Fig. 6) and negative values of $T_{IV} = -2\overline{(\partial u_k/\partial x_k)\Omega}$ (see Fig. 4) at all stages of head-on interaction in the case of the adiabatic wall. By contrast, the isotherms move away from the wall after flame quenching in the isothermal case,[40] which

gives rise to predominantly negative values of $S_\theta = (D\theta/Dt)/|\nabla\theta|$ leading to negative values of $\partial u_i/\partial x_i = \tau\rho S_\theta|\nabla\theta|/\rho_0$ at the final stages of head-on interaction, which can be substantiated from negative values of $\overline{\partial u_i/\partial x_i}$ in the isothermal case at $t/t_f = 16.27$ in Fig. 6.

The density gradient induced by heat release also affects the baroclinic torque contribution $T_V = \vec{\omega} \cdot (\nabla\rho \times \nabla p)/\rho^2$. The density gradient $\nabla\rho = -\tau\rho^2\nabla\theta/\rho_0$ can be expressed as $\nabla\rho = \vec{N}_\theta\tau\rho^2|\nabla\theta|/\rho_0$ where $\vec{N}_\theta = -\nabla\theta/|\nabla\theta|$ is the normal vector on a non-dimensional temperature isosurface. In the case of low Mach number and unity Lewis number conditions without heat loss, which is the case when the flame is away from the wall, the normal vector $\vec{N}_\theta$ remains collinearly aligned with $\vec{N} = -\nabla c/|\nabla c|$ due to $c \approx \theta$,[11] but this collinear alignment decreases during flame-wall interaction in the isothermal case due to $c \neq \theta$. However, the collinearity between $\vec{N}_\theta$ and $\vec{N}$ is maintained in the case of the adiabatic wall. A comparison between $\overline{|\nabla\rho|} \times \delta_{th}/\rho_0$ and $\vec{N} \cdot \nabla\rho \times \delta_{th}/\rho_0 = \vec{N} \cdot \vec{N}_\theta\tau\rho^2|\nabla\theta|/\rho_0 \times \delta_{th}/\rho_0$ in Fig. 6 reveals that $\overline{|\nabla\rho|}$ remains identical to $\vec{N} \cdot \nabla\rho$ in the case of an adiabatic wall, whereas these two quantities remain close to each other in the isothermal case although the strict equality is not maintained. This further suggests that $\vec{N} \cdot \vec{N}_\theta$ remains close to unity even in the isothermal wall boundary condition at all stages of flame-wall interaction. The above findings suggest that the density gradient $\nabla\rho$ aligns with the temperature gradient and approximately (identically) with the flame normal vector for isothermal (adiabatic) boundary condition, and thus the baroclinic torque contribution $T_V = \vec{\omega} \cdot (\nabla\rho \times \nabla p)/\rho^2$ arises due to the pressure gradient component which is tangential to the isotherms (or to the flame surface).

The wall-normal variations of the normalized pressure gradient magnitude $\overline{|\nabla p|} \times \delta_{th}/\rho_0 u_{\tau,NR}^2$ and the normalized flame-normal pressure gradient magnitude $\overline{|\vec{N} \cdot \nabla p|} \times \delta_{th}/\rho_0 u_{\tau,NR}^2$ are shown in Fig. 8 at different time instants during head-on interaction. Figure 8 shows that there are significant differences between $\overline{|\nabla p|}$ and $\overline{|\vec{N} \cdot \nabla p|}$ when the flame remains away of the wall, but this difference decreases with time as the head-on interaction progresses. This suggests that there is a significant pressure gradient in the flame tangential direction when the flame is either away from the wall (e.g., $t/t_f = 3.99$) or starts to interact with the wall (e.g., $t/t_f = 10.92$), which can induce a significant amount of baroclinic torque $\nabla\rho \times \nabla p$ and accordingly T_V plays a leading order role within the flame brush. However, the magnitude and influence of the baroclinic term T_V weakens with the progress of head-on interaction due to the reduced influence of pressure gradient in the flame-tangential direction (see Fig. 8).

The pressure gradient in the flame normal direction is induced by the flame normal acceleration due to thermal expansion and that in the flame tangential direction is induced by the flame wrinkling,[10,11] which can be quantified by the departure of $|\vec{N} \cdot \vec{n}_w|$ from unity where $\vec{n}_w$ is the wall normal vector which is orientated opposite to the direction of mean flame propagation. The probability density functions (PDFs) of $|\vec{N} \cdot \vec{n}_w|$ in the region given by $0.01 < c < 0.99$ at different time instants are shown for both isothermal and adiabatic boundary conditions in Fig. 9. The PDFs of $\cos\theta_p = \vec{\omega} \cdot (\nabla\rho \times \nabla p)/(|\vec{\omega}||\nabla\rho \times \nabla p|)$ in the region given by $0.01 < c < 0.99$ at different
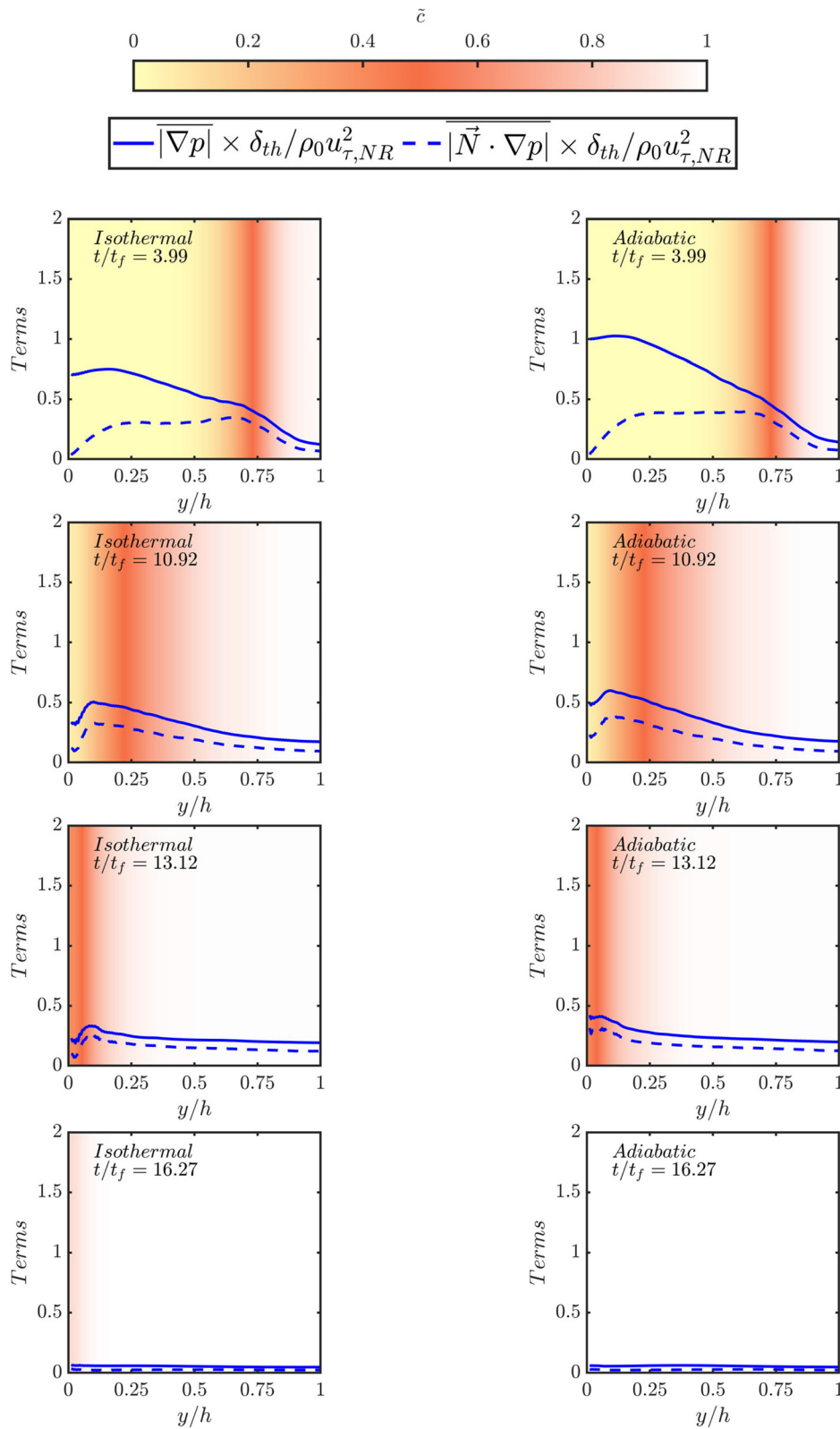
FIG. 8. Variations of the normalized pressure gradient magnitude $\overline{|\nabla p|} \times \delta_{th}/\rho_0 u_{\tau,NR}^2$ and the normalized flame-normal pressure gradient magnitude $\overline{|\vec{N} \cdot \nabla p|} \times \delta_{th}/ \rho_0 u_{\tau,NR}^2$ with the normalized wall normal distance y/h for isothermal (left) and adiabatic (right) wall boundary conditions at $t/t_f = 3.99$, 10.92, 13.12, and 16.27 (top to bottom).

time instants are also shown for both isothermal and adiabatic boundary conditions in Fig. 9, which shows that $\cos\theta_p$ predominantly assumes positive values suggesting that the baroclinic torque $\nabla\rho \times \nabla p$ acts to generate vorticity in both cases, which is consistent with previous findings.[10,11] The results from Fig. 9 indicate that the flame wrinkling tends to decrease with the progress of head-on interaction, which leads to weakening the magnitude of the pressure gradient in the flame-tangential direction and T_V contribution to the enstrophy transport. The statistics at $t/t_f = 16.27$ are purposely not shown in Fig. 9 because the gradients of density and reaction progress variable vanish at $t/t_f = 16.27$ due to the disappearance of the flame by that stage.

Finally, it is worthwhile to consider the statistical behaviors of the vortex-stretching and the combined diffusion and dissipation contributions (i.e., T_I and T_{III}), which are leading source and sink terms in the enstrophy transport equation, respectively. The vortex-stretching term T_I can be expressed as[9,15,16,19]

$$T_I = \overline{2\Omega\left(s_\alpha\cos^2\theta_\alpha + s_\beta\cos^2\theta_\beta + s_\gamma\cos^2\theta_\gamma\right)}, \quad (5)$$

where s_α, s_β, and s_γ are the most extensive, intermediate, and the most compressive principal strain rate, and $\theta_\alpha, \theta_\beta$, and θ_γ are the angles between $\vec{\omega}$ and eigenvectors associated with s_α, s_β, and s_γ, respectively. It was reported in several previous analyses[8,9,15] that $\vec{\omega}$ predominantly aligns with the eigenvector associated with s_β in premixed flames.

The variations of $\overline{|\cos\theta_\alpha|}$, $\overline{|\cos\theta_\beta|}$, and $\overline{|\cos\theta_\gamma|}$ in the wall-normal direction are shown in Fig. 10, which shows $\overline{|\cos\theta_\beta|}$ assumes higher values than $\overline{|\cos\theta_\alpha|}$ and $\overline{|\cos\theta_\gamma|}$, indicating a preferential alignment with the eigenvector associated with s_β. This is qualitatively similar to the behavior reported by Bechlars and Sandberg[7] for non-reacting turbulent boundary layers. As s_β is predominantly positive,[7,9,22] the mean vortex-stretching term T_I assumes positive values at all stages of head-on interaction irrespective of the wall boundary condition. As the magnitudes of strain rates s_α, s_β, and s_γ and enstrophy Ω decrease with the progress of flame-wall interaction, the magnitude of T_I drops with time.

The term T_{III} can be expanded as[19,22]

$$T_{III} = \overline{(\mu/\rho)\nabla^2\Omega} + \overline{(\mu/3\rho)\vec{\omega}\cdot[\nabla\times\nabla(\nabla\cdot\vec{u})]} + f(\mu) - D_\nu, \quad (6)$$

where $f(\mu)$ represents the contributions from viscosity gradients and $-D_\nu = -\overline{(\mu/\rho)(\partial\omega_i/\partial x_l)(\partial\omega_i/\partial x_l)}$ is the molecular dissipation of enstrophy, whereas the second term on right hand side of Eq. (6) vanishes according to the mathematical identity $\nabla\times\nabla(\nabla\cdot\vec{u}) = 0$.

The variations of T_{III} and $(-D_\nu)$ in the wall normal direction are shown in Fig. 11, which shows that the magnitude of $(-D_\nu)$ remains close to that of T_{III} for $y/h > 0.3$, indicating that the contribution of $\overline{[(\mu/\rho)\nabla^2\Omega + f(\mu)]}$ remains small in comparison to $(-D_\nu)$ in this region at all stages of head-on interaction for both wall boundary
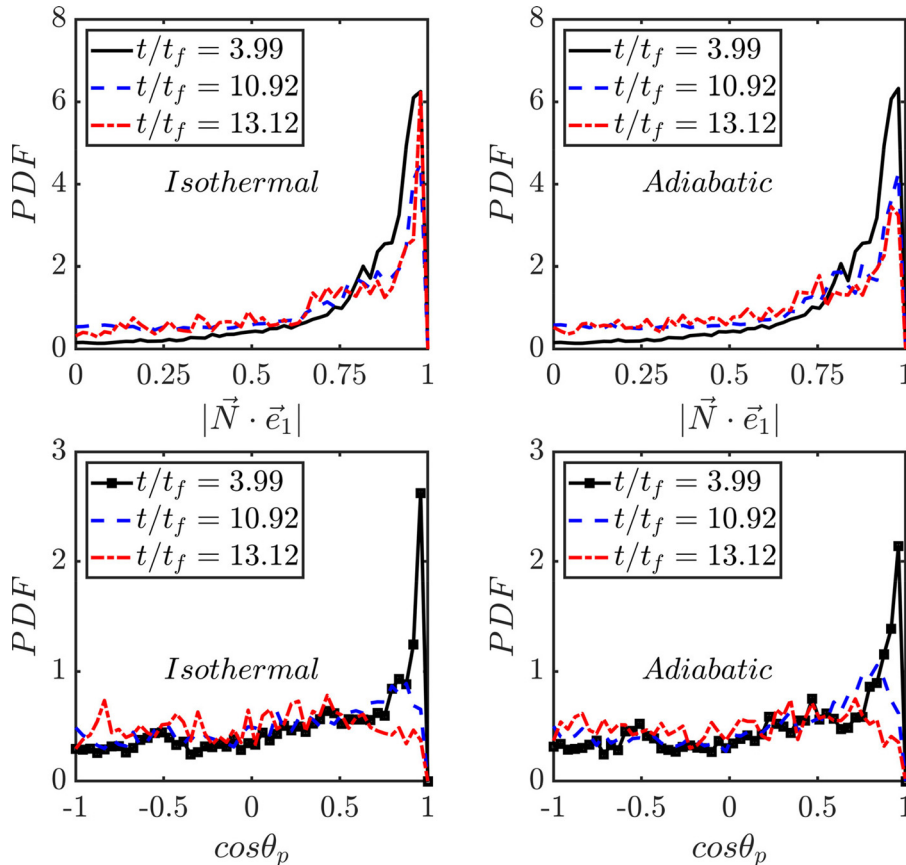

FIG. 9. PDFs of $|\vec{N}\cdot\vec{n}_w|$ and $\cos\theta_p = \vec{\omega}\cdot(\nabla\rho\times\nabla p)/(|\vec{\omega}||\nabla\rho\times\nabla p|)$ in the reaction progress variable range given by $0.01 < c < 0.99$ for isothermal (left) and adiabatic (right) wall boundary conditions at $t/t_f = 3.99$, 10.92, 13.12, and 16.27 (top to bottom).
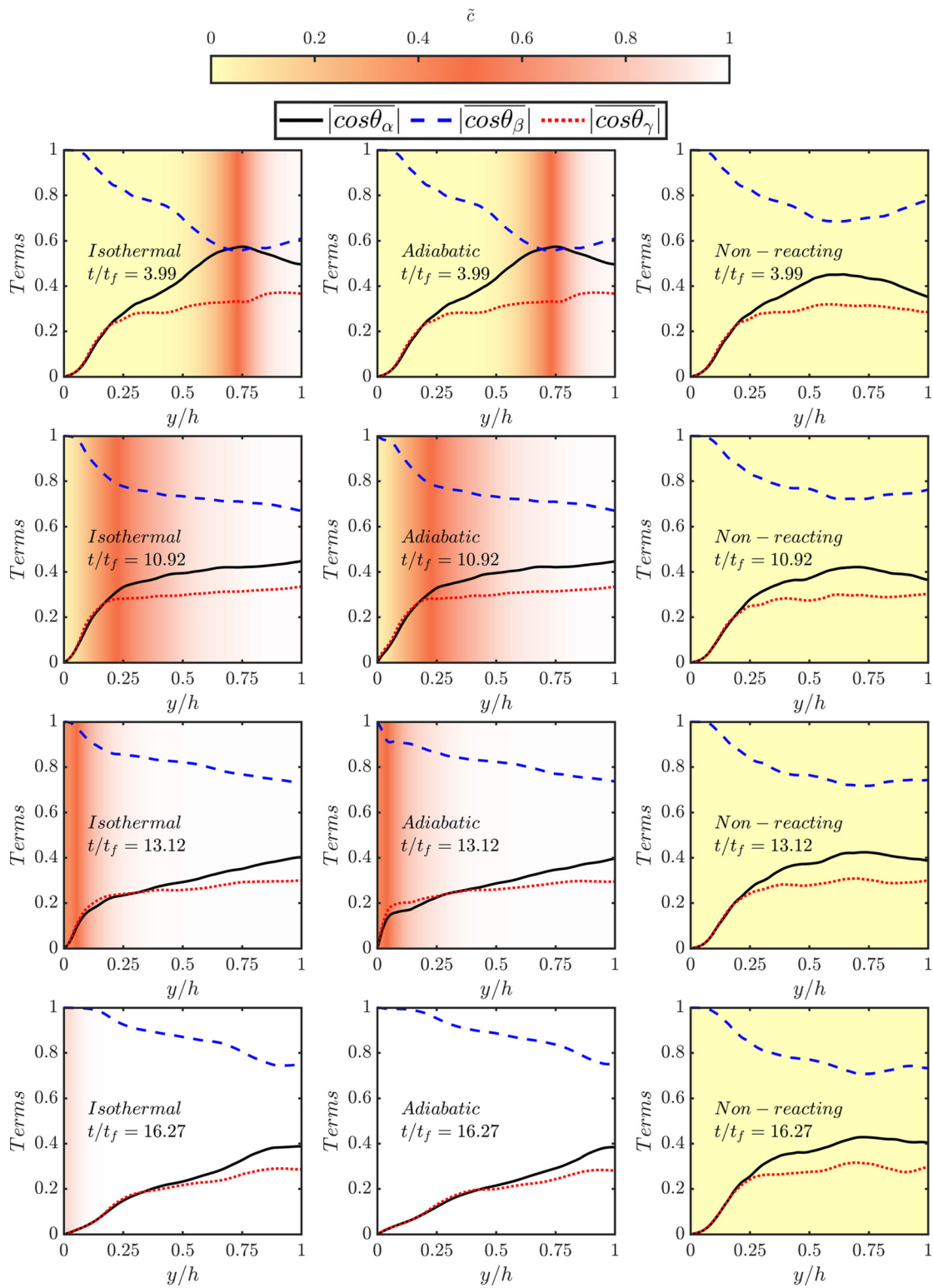
FIG. 10. Variations of $\overline{|\cos\theta_\alpha|}$, $\overline{|\cos\theta_\beta|}$, and $\overline{|\cos\theta_\gamma|}$ with the normalized wall normal distance y/h for isothermal (left), adiabatic (middle), and non-reacting (right) wall boundary conditions at $t/t_f = 3.99$, 10.92, 13.12, and 16.27 (top to bottom).
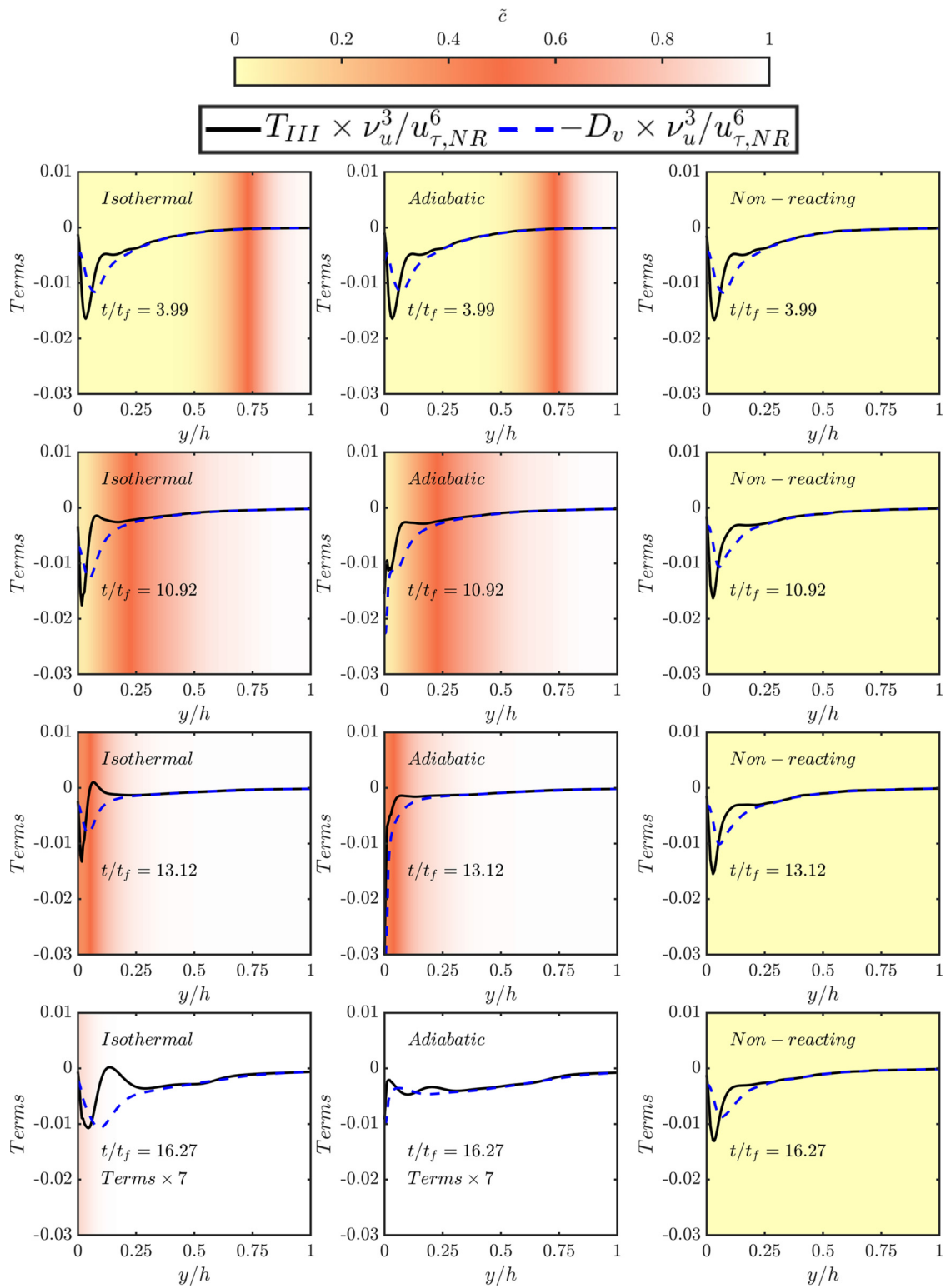
FIG. 11. Variations of $T_{III} \times \nu_u^3/u_{\tau,NR}^6$ and $(-D_v) \times \nu_u^3/u_{\tau,NR}^6$ with the normalized wall normal distance y/h for isothermal (left), adiabatic (middle) and non-reacting (right) wall boundary conditions at $t/t_f = 3.99$, 10.92, 13.12, and 16.27 (top to bottom).
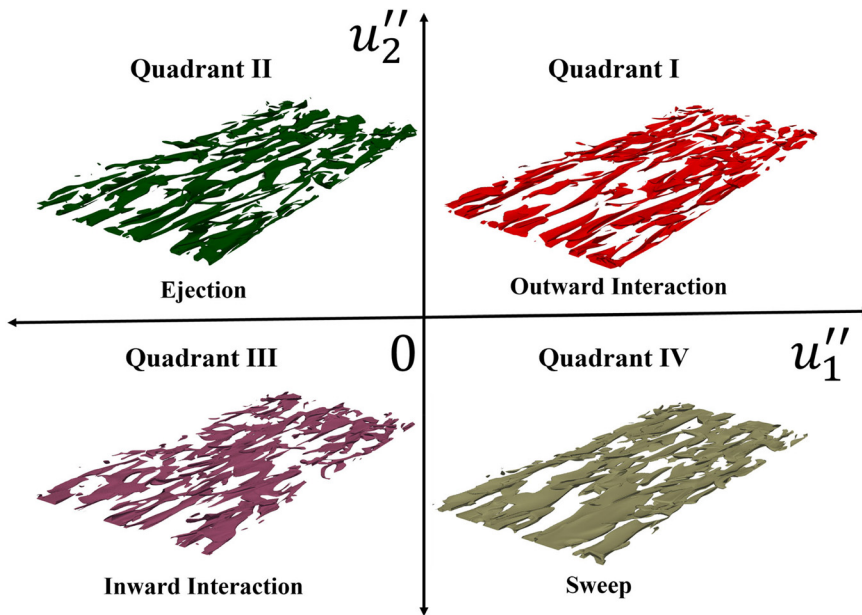
FIG. 12. Different coherent structures in turbulent boundary layers characterized by outward interactions (i.e., quadrant I: $u_1'' > 0$ and $u_2'' > 0$), ejection (i.e., quadrant II: $u_1'' < 0$ and $u_2'' > 0$), inward interactions (i.e., quadrant III: $u_1'' < 0$ and $u_2'' < 0$), and sweep (i.e., quadrant IV: $u_1'' > 0$ and $u_2'' < 0$).

conditions. However, there are significant quantitative differences between T_{III} and $(-D_\nu)$ close to the wall (i.e., $y/h < 0.3$) and there can also be qualitative differences at the final stages of head-on interaction (e.g., $t/t_f = 16.27$). The drop in the magnitude of vorticity components with the progress of head-on interaction leads to a drop in T_{III} and its components with time.

Finally, it is worth investigating the enstrophy magnitudes for different coherent structures characterized by different quadrants, namely, outward interactions (i.e., quadrant I: $u_1'' > 0$ and $u_2'' > 0$), ejection (i.e., quadrant II: $u_1'' < 0$ and $u_2'' > 0$), inward interactions (i.e., quadrant III: $u_1'' < 0$ and $u_2'' < 0$), and sweep (i.e., quadrant IV: $u_1'' > 0$ and $u_2'' < 0$), as shown in Fig. 12.[39,63] Figure 13 shows the instantaneous distribution of different coherent structures present on

the $x - y$ plane at $z/h = 4$. It is evident from Fig. 13 that the distribution of the coherent structures does not change significantly in comparison to the non-reacting flow when the flame is significantly away from the wall (i.e., $t/t_f = 3.99$) and mostly ejections and sweep events are the dominant structures for both wall boundary conditions. Figure 13 suggests that the ejections and sweeps are the dominant flow structures in the non-reacting channel flow for all instants in time, but the occurrences of inward and outward interactions increase significantly in the reacting cases with the progress of head-on interaction. Moreover, the wall boundary condition does not seem to have any major influence on the flow structure in the reacting cases. These observations can be substantiated in terms of the probabilities of obtaining different coherent structures at different time instants in Fig. 14. It can be seen
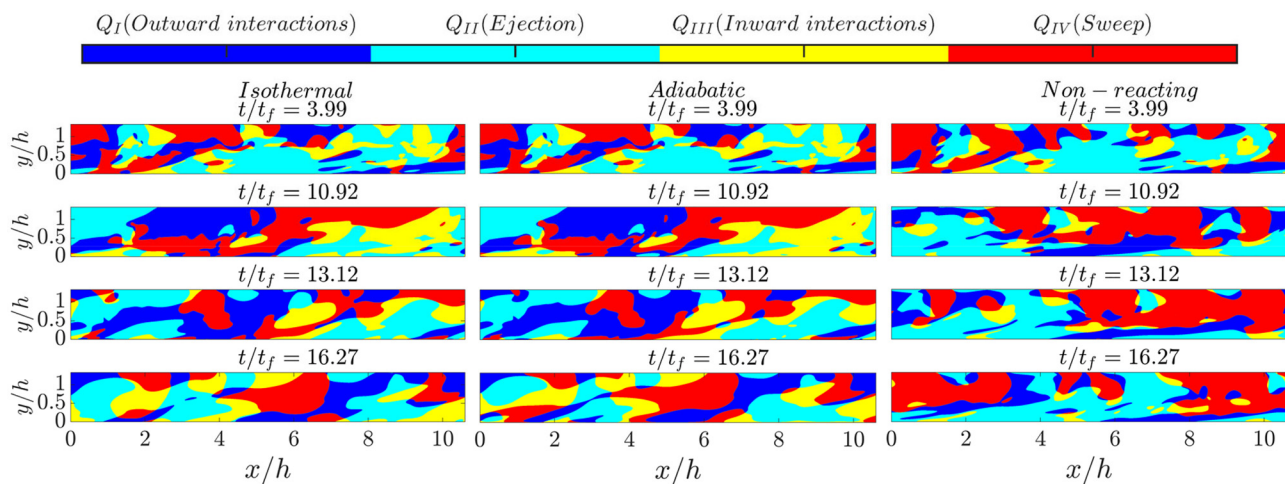

FIG. 13. Variations of $\langle \Omega \rangle_\alpha \times \nu_u^2 / u_{\tau,NR}^4$ (where $\alpha = I, II, III,$ and IV) and $\overline{\Omega} \times \nu_u^2 / u_{\tau,NR}^4$ with the normalized wall normal distance y/h for isothermal (left) and adiabatic (right) wall boundary conditions at $t/t_f = 3.99$, 10.92, 13.12, and 16.27 (top to bottom).
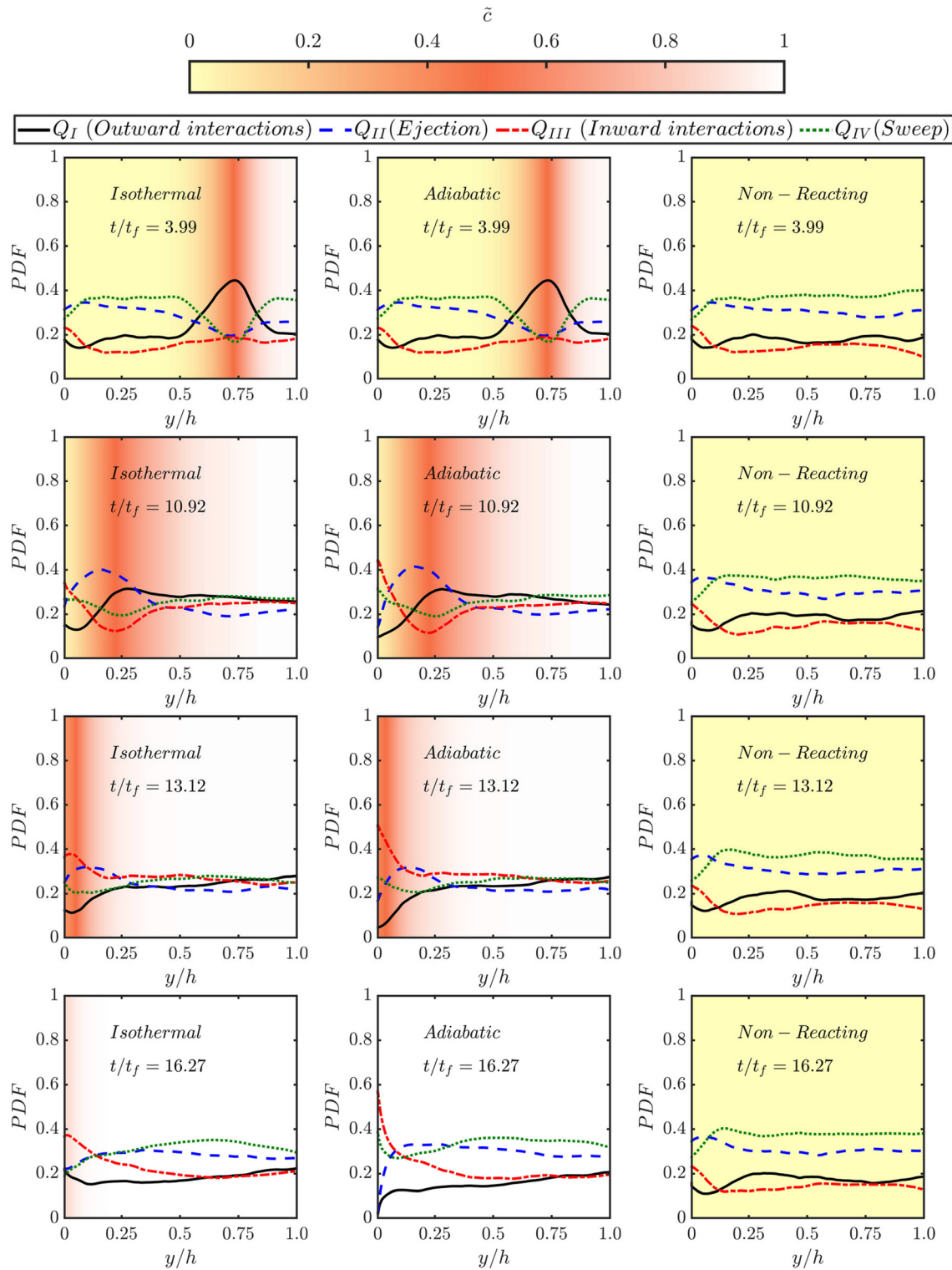
FIG. 14. Variations of the probabilities of Q_I (i.e., $u_1'' > 0$ and $u_2'' > 0$), Q_{II} (i.e., Q_{II}: $u_1'' < 0$ and $u_2'' > 0$), Q_{III} (i.e., $u_1'' < 0$ and $u_2'' < 0$), and Q_{IV} (i.e., $u_1'' > 0$ and $u_2'' < 0$) with y/h for isothermal (left), adiabatic (middle) wall boundary conditions and non-reacting conditions (right) at $t/t_f = 3.99$, 10.92, 13.12, and 16.27 (top to bottom). Please note that the first grid point is not plotted in Figs. 14–19 because quadrants do not have any physical meaning at the wall due to the no-slip boundary condition.
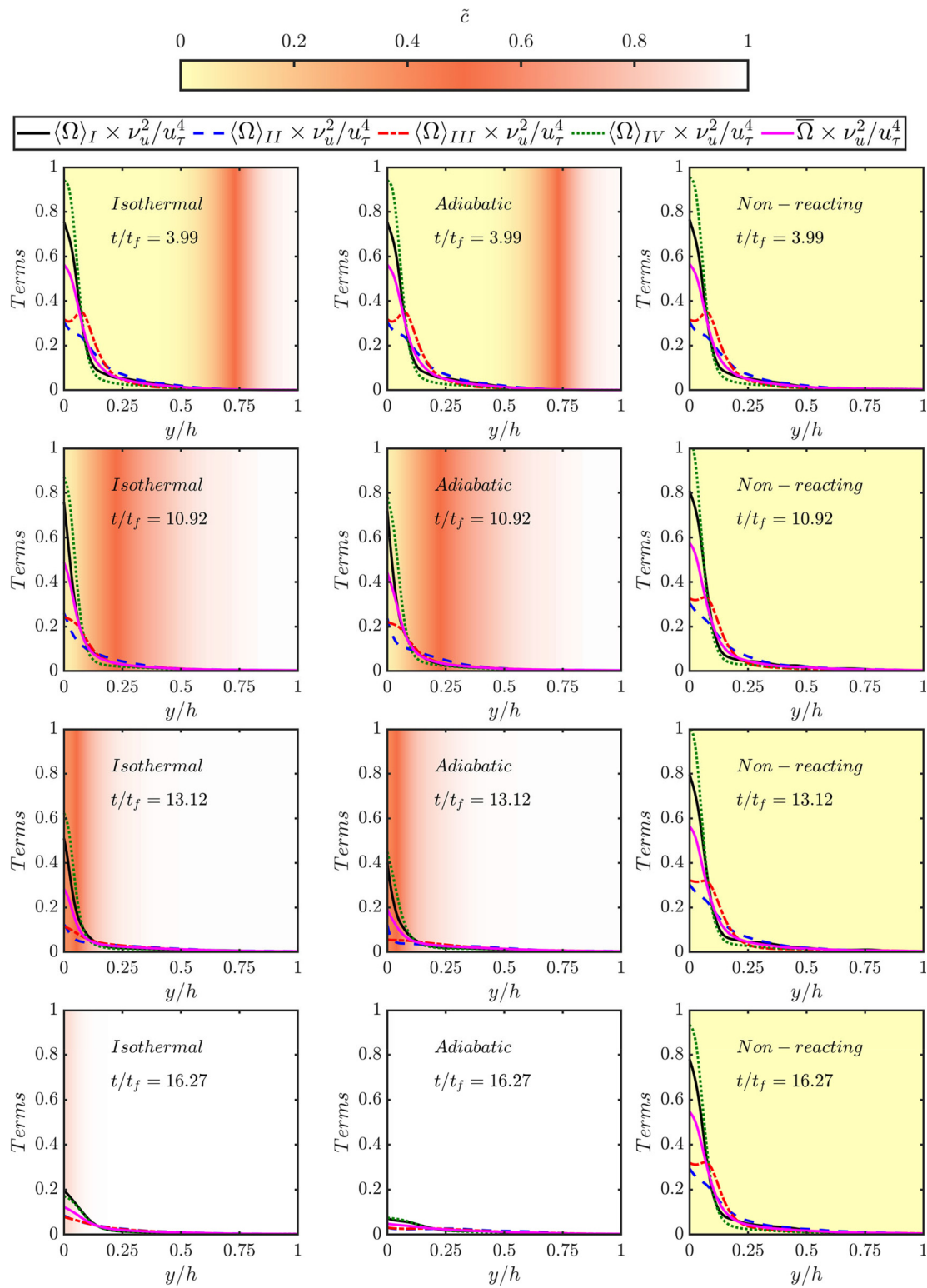
FIG. 15. Variations of $\langle\Omega\rangle_\alpha \times \nu_u^2/u_{\tau,NR}^4$ (where $\alpha = I, II, III,$ and IV) and $\overline{\Omega} \times \nu_u^2/u_{\tau,NR}^4$ with the normalized wall normal distance y/h for isothermal (left), adiabatic (middle) wall boundary conditions, and non-reacting conditions (right) at $t/t_f = 3.99, 10.92, 13.12,$ and 16.27 (top to bottom).
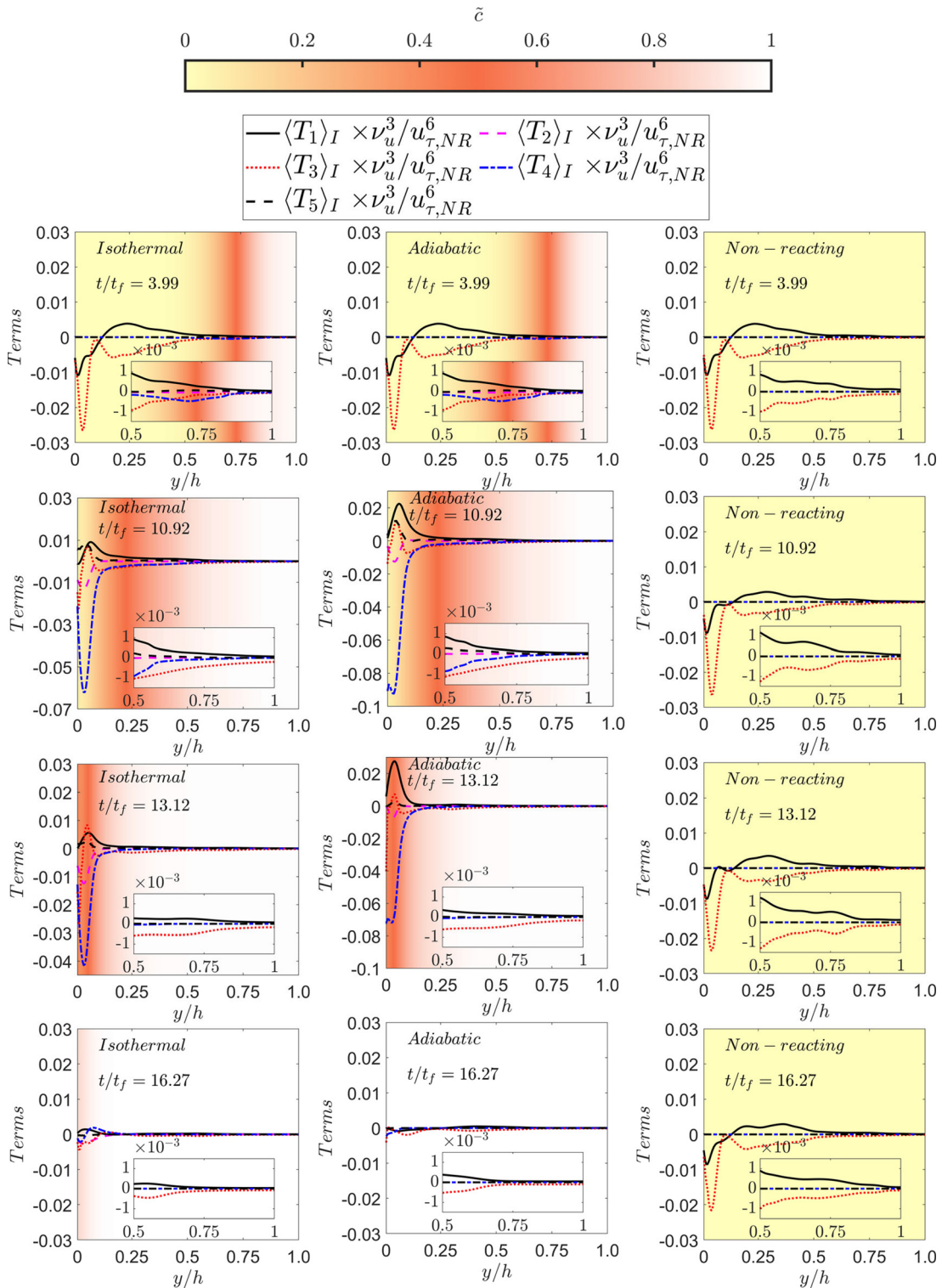
FIG. 16. Variations of the normalized source/sink terms of the enstrophy transport equation conditioned on quadrant I (i.e., $\{\langle T_1 \rangle_I, \langle T_2 \rangle_I, \langle T_3 \rangle_I, \langle T_4 \rangle_I, \text{and } \langle T_5 \rangle_I\} \times \nu_u^3/u_{\tau,NR}^6$) with the normalized wall normal distance y/h for isothermal (left) and adiabatic (middle) wall boundary conditions and the non-reacting configuration (right) at $t/t_f = 3.99$, 10.92, 13.12, and 16.27 (top to bottom).
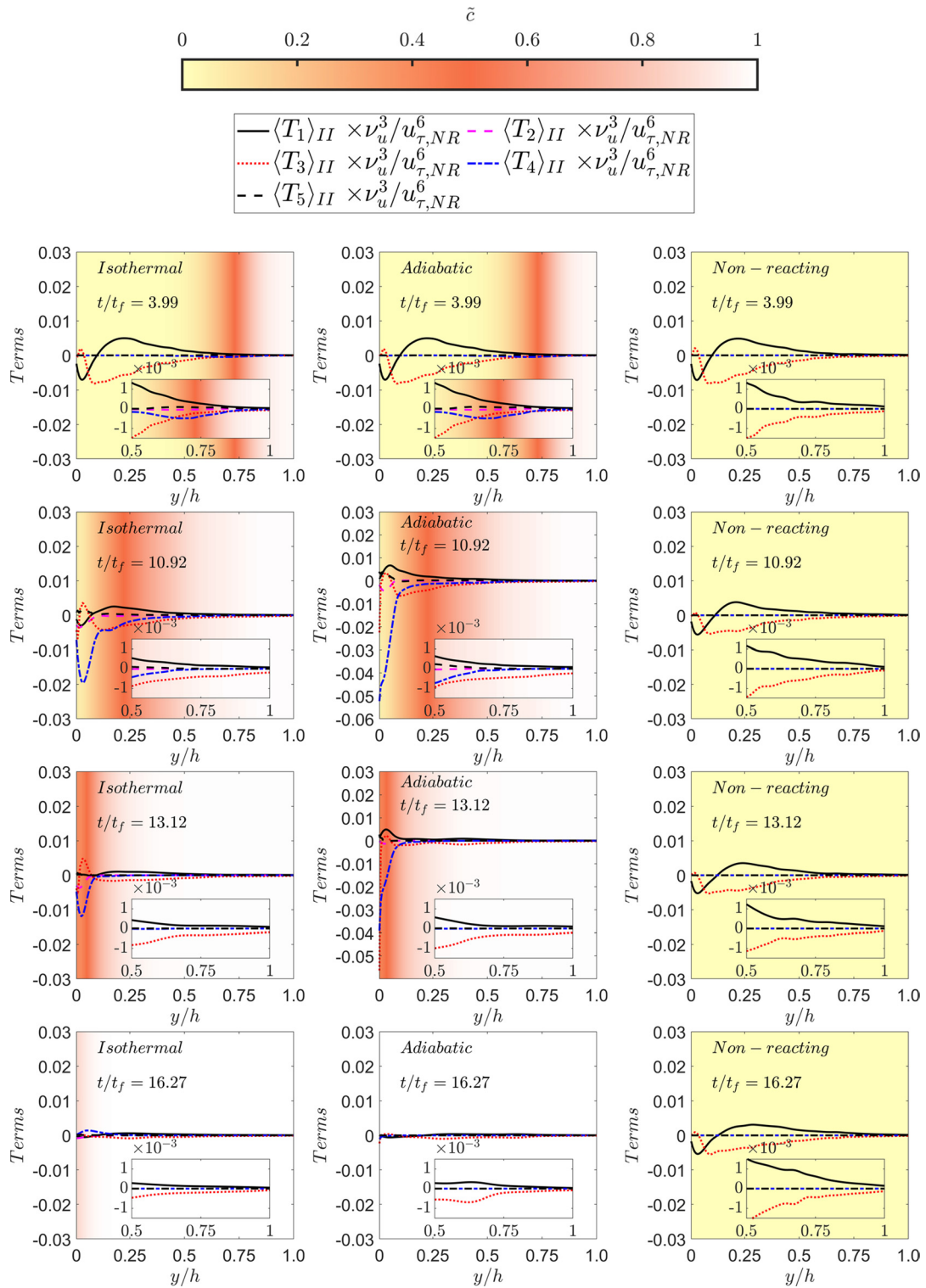
FIG. 17. Variations of the normalized source/sink terms of the enstrophy transport equation conditioned on quadrant II (i.e., $\{\langle T_1 \rangle_{II}, \langle T_2 \rangle_{II}, \langle T_3 \rangle_{II}, \langle T_4 \rangle_{II},$ and $\langle T_5 \rangle_{II}\} \times \nu_u^3 / u_{\tau,NR}^6$) with the normalized wall normal distance y/h for isothermal (left) and adiabatic (middle) wall boundary conditions and the non-reacting configuration (right) at $t/t_f = 3.99, 10.92, 13.12,$ and 16.27 (top to bottom).

FIG. 18. Variations of the normalized source/sink terms of the enstrophy transport equation conditioned on quadrant III (i.e., $\{\langle T_1 \rangle_{III}, \langle T_2 \rangle_{III}, \langle T_3 \rangle_{III}, \langle T_4 \rangle_{III}$, and $\langle T_5 \rangle_I\} \times \nu_u^3/u_{\tau,NR}^6$) with the normalized wall normal distance y/h for isothermal (left) and adiabatic (middle) wall boundary conditions and the non-reacting configuration (right) at $t/t_f = 3.99$, 10.92, 13.12, and 16.27 (top to bottom).
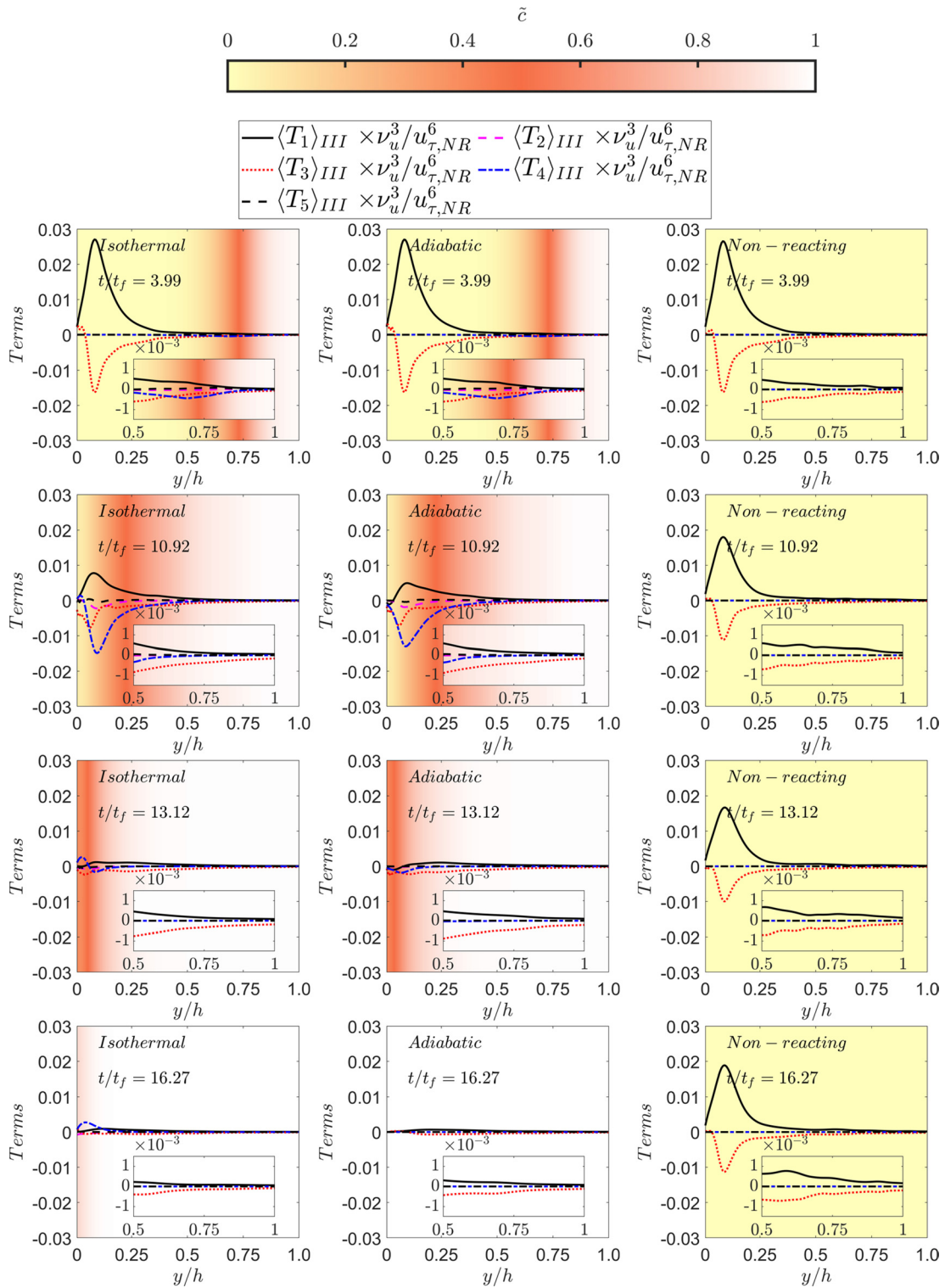
FIG. 19. Variations of the normalized source/sink terms of the enstrophy transport equation conditioned on quadrant IV (i.e., $\{\langle T_1 \rangle_{IV}, \langle T_2 \rangle_{IV}, \langle T_3 \rangle_{IV}, \langle T_4 \rangle_{IV}$, and $\langle T_5 \rangle_{IV}\} \times \nu_u^3/u_{\tau,NR}^6$) with the normalized wall normal distance y/h for isothermal (left) and adiabatic (middle) wall boundary conditions and the non-reacting configuration (right) at $t/t_f = 3.99$, 10.92, 13.12, and 16.27 (top to bottom).
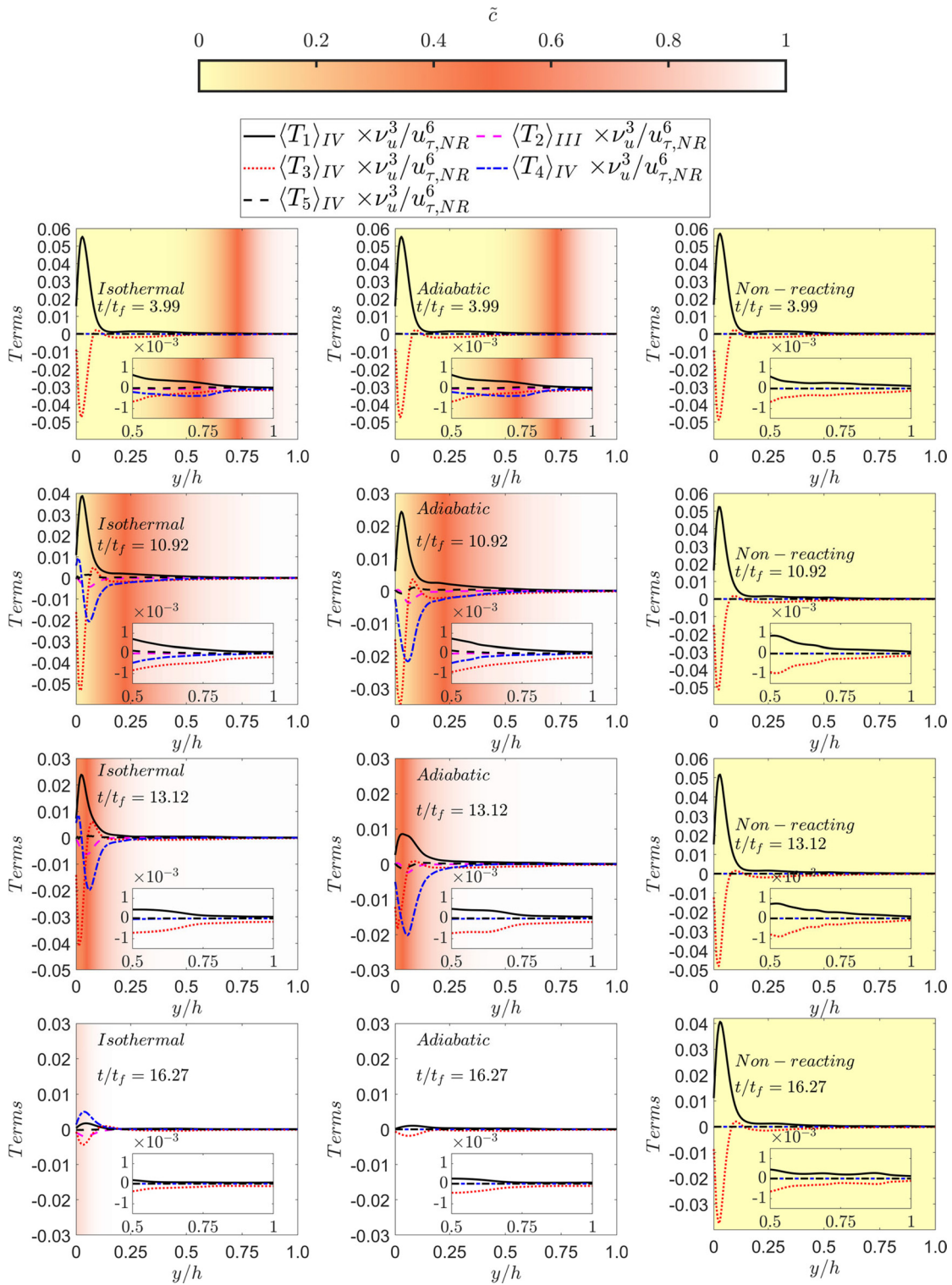
from Fig. 14 that the presence of the flame increases the likelihood of obtaining outward interactions at the expense of sweep and ejections in the region of the flame brush where the effects of thermal expansion are strong (i.e., high values of $\overline{\partial u_i / \partial x_i}$, see Fig. 6) when the flame is away from the wall (e.g., $t/t_f = 3.99$). Moreover, the likelihood of obtaining ejections, sweeps, and inward interactions remains comparably close to the wall with the progress of flame-wall interaction (e.g., $t/t_f = 10.92$ and 13.12) under reacting conditions due to thermal expansion effects as the mean direction of flame propagation is aligned with the wall normal direction, and all the four coherent structures have comparable probabilities away from the wall. The qualitative nature of this behavior is not affected by the wall boundary condition. Furthermore, when the flame reaches close to extinction at $t/t_f = 16.27$, the probability of finding inward interactions remains high close to the wall but ejections and sweeps remain the dominant structures away from the wall, which is qualitatively similar to the non-reacting flow where the probability of finding ejections and sweeps remain high at all locations at all times. These differences in probabilities of coherent structures have implications in terms of statistical behaviors and modeling of Reynolds stresses[55] $\overline{\rho u_1'' u_2''}$ in the flame-wall interaction within turbulent boundary layers, which is beyond the scope of current analysis but will be addressed in the future.

The wall normal variations of mean value of the normalized enstrophy $\langle \Omega \rangle_\alpha \times \nu_u^2 / u_{\tau,NR}^4$ (where $\alpha = I, II, III$, and IV and the angled bracket is the mean value conditional upon a given quadrant) conditional upon coherent structures are shown in Fig. 15 at different time instants. Figures 14 and 15 show that the probability of finding sweep and ejection events which are associated with $u_1'' u_2'' < 0$ remain greater than the outward and inward interactions for which $u_1'' u_2'' > 0$ in the non-reacting flow, but the mean enstrophy conditional upon outward interactions and sweep (i.e., $\langle \Omega \rangle_I$ and $\langle \Omega \rangle_{IV}$) are found to be greater than those due to ejection and inward interactions (i.e., $\langle \Omega \rangle_{II}$ and $\langle \Omega \rangle_{III}$) in this case. The same qualitative behavior is observed for the reactive cases at all times for both wall boundary conditions, but $\langle \Omega \rangle_\alpha \times \nu_u^2 / u_{\tau,NR}^4$ (for $\alpha = I, II, III$, and IV) decreases with the progress of head-on flame-wall interaction. Outward interactions and sweep are characterized by $u_1'' > 0$ and the axial velocity component carries the largest part of turbulent kinetic energy. Thus, the regions of large turbulent kinetic energy seem to be associated with regions of large dissipation rate, which is consistent with the observation for constant density conditions (e.g., $\overline{\rho \tilde{\varepsilon}} \sim 2\mu \overline{\Omega}$).[39]

Figures 16–19 show the wall normal variations of the mean values of the different terms of the enstrophy transport equation conditional upon coherent structures (i.e., $\langle T_1 \rangle_\alpha, \langle T_2 \rangle_\alpha, \langle T_3 \rangle_\alpha, \langle T_4 \rangle_\alpha$, and $\langle T_5 \rangle_\alpha$). It can be seen from Figs. 16–19 that the variations of $\langle T_1 \rangle_\alpha, \langle T_2 \rangle_\alpha, \langle T_3 \rangle_\alpha, \langle T_4 \rangle_\alpha$, and $\langle T_5 \rangle_\alpha$ (for $\alpha = I, II, III$, and IV) within the flame brush are qualitatively similar to the corresponding terms in the transport equation of $\overline{\Omega}$ (i.e., $T_I, T_{II}, T_{III}, T_{IV}$, and T_V). However, $\langle T_1 \rangle_\alpha$ acts close to the wall as a sink term for $\alpha = I$ and II but remains a source term for $\alpha = III$ and IV for the non-reacting flow at all times and when the flame is away from the wall $(t/t_f = 3.99)$. Moreover, with the advance of head-on interaction, the contribution of $\langle T_3 \rangle_\alpha$ assumes positive values close to the wall for $\alpha = I$ and II due to the diffusion contribution $\langle (\mu/\rho)\nabla^2 \Omega \rangle_\alpha$ and this trend can also be discerned for $\alpha = III$ and IV but it is much weaker than for $\alpha = I$ and II. Moreover, the transport behavior of $\langle T_1 \rangle_\alpha, \langle T_2 \rangle_\alpha, \langle T_4 \rangle_\alpha$, and $\langle T_5 \rangle_\alpha$ for $\alpha = III$ and IV are found to be

qualitatively similar to the corresponding terms in the transport equation of $\overline{\Omega}$.

V. CONCLUSIONS

The statistical behaviors of mean enstrophy and its evolution during head-on interaction of premixed flames propagating toward a chemically inert flat wall across the turbulent boundary layer have been analyzed using DNS data for both isothermal and adiabatic thermal wall boundary conditions for a friction velocity-based Reynolds number of $Re_\tau = 110$. It has been found that the mean enstrophy distribution within turbulent boundary layer is significantly affected by the thermal expansion induced by the heat release due to combustion. The contributions of vortex-stretching and viscous dissipation are found to be leading order source and sink, respectively, to the mean enstrophy transport under both reacting and non-reacting conditions. It has been found that the dilatation rate and baroclinic torque contributions arising from thermal expansion play important roles in addition to the leading order contributions of the vortex-stretching and viscous dissipation terms in the enstrophy transport equation in the case of premixed flame-wall interaction. The magnitudes of the leading order contributors to the enstrophy transport decrease with time as head-on interaction progresses for both wall boundary conditions. The overall sink contributions to the enstrophy transport dominate over the source contributions leading to a drop in the mean enstrophy with time due to the progress of head-on interaction. The dilatation contribution in the vicinity of the wall is affected by the thermal boundary condition, which, in turn, affects the near-wall distribution of enstrophy. Therefore, enstrophy distribution within the turbulent boundary layer changes significantly during flame-wall interaction, which is reflected in the modification of the relative proportion of the coherent structures in the reacting flow turbulent boundary layer in comparison to the corresponding non-reacting flow. It has been demonstrated that the distribution of coherent structures within the boundary layer is significantly altered due to the presence of the flame, which may have a significant influence on the distribution and modeling of Reynolds stresses in reacting flow turbulent boundary layer when compared to that in the corresponding non-reacting flow boundary layer. Thus, the turbulence modeling of non-reacting flows (e.g., modeling of Reynolds stresses) might not be valid during flame-wall interaction within turbulent boundary layers.

The statistics of mean enstrophy and the terms of its transport equation reveal that the flow structure in the reacting flow turbulent boundary layer is fundamentally different from the non-reacting flow turbulent boundary layer. The dilatation rate arising from heat release in premixed turbulent combustion acts to decrease the enstrophy magnitude, and this trend strengthens with the progress of flame-wall interaction. The thermal wall boundary condition influences the dilatation contribution in the vicinity of the wall, which in turn affect the near-wall distribution of enstrophy. The enstrophy distribution within the turbulent boundary layer changes significantly during the head-on interaction, which modifies the relative proportion of the coherent structures in the reacting flow turbulent boundary layer in comparison to the corresponding non-reacting flow. This further suggests that the modeling of Reynolds stresses $\overline{\rho u_1'' u_2''}$ needs to be modified for the simulation of flame-wall interaction in turbulent boundary layers, which is beyond the scope of this analysis but will form the basis of future investigations. Moreover, the current simple chemistry analysis focuses on the fluid-dynamical aspects of head-on interaction of

premixed flames in turbulent boundary layers and thus the findings of this analysis need to be confirmed in the presence of detailed chemistry although the vorticity dynamics obtained from simple chemistry DNS[10,15] has been found to be qualitatively similar to the corresponding detailed chemistry DNS results.[18,56] The effects of Re_τ and Lewis number on the enstrophy statistics in premixed flame-wall interaction in turbulent boundary layers need to be investigated further and will form the platform for future investigations.

AUTHOR DECLARATIONS
Conflict of Interest

The authors have no conflicts to disclose.

Author Contributions

Sanjeev Ghai: Data curation (supporting); Formal analysis (supporting); Software (supporting); Visualization (equal). **Nilanjan Chakraborty:** Conceptualization (lead); Data curation (equal); Funding acquisition (lead); Resources (lead); Software (lead); Supervision (lead); Writing – original draft (lead); Writing – review and editing (lead). **Umair Ahmed:** Conceptualization (supporting); Data curation (lead); Formal analysis (supporting); Software (supporting); Supervision (supporting); Visualization (supporting); Writing – original draft (supporting); Writing – review and editing (supporting). **Markus Klein:** Conceptualization (supporting); Funding acquisition (lead); Resources (supporting); Writing – original draft (supporting); Writing – review and editing (supporting).

DATA AVAILABILITY

The data that support the findings of this study are available from the corresponding author upon reasonable request.

APPENDIX: COMPARISON WITH PREVIOUS DNS AND EXPERIMENTAL RESULTS

Figure 20 shows the variation of $\overline{\rho\tilde{\varepsilon}}/2\mu_u \times \nu_u^2/u_{\tau,NR}^4$ with the normalized wall normal distance y^+ for the non-reacting case at $t/t_f = 3.99$, which are also compared to previous DNS results of fully developed turbulent channel flow solution[6] at $Re_\tau = 145$ and experimental measurements[54] of flow over a flat plate for $Re_\tau = 890$. It can be seen from Fig. 20 that the distribution of $\overline{\rho\tilde{\varepsilon}}/2\mu_u \times \nu_u^2/u_{\tau,NR}^4$ for the non-reacting flow case considered here remains in good quantitative agreement with DNS results by Gorski et al.[6] and also in good qualitative agreement with experimental measurements of Balint et al.[65] The quantitative differences between the present simulation results and previous findings[6,65] can be attributed to the differences in Re_τ values. It can further be seen from Fig. 20 that $\overline{\rho\tilde{\varepsilon}}/2\mu$ remains in good agreement with $\overline{\omega_i'\omega_i'}/2$. Moreover, $\overline{\omega_i}\,\overline{\omega_i}/2 > \overline{\omega_i'\omega_i'}/2$ is
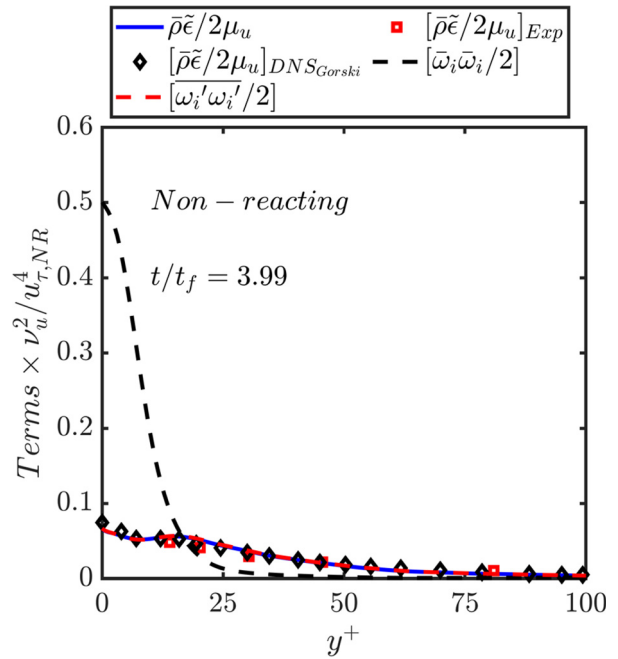

FIG. 20. Variations of $\overline{\rho\tilde{\varepsilon}}/2\mu_u \times \nu_u^2/u_{\tau,NR}^4$, $[\overline{\omega_i}\,\overline{\omega_i}/2] \times \nu_u^2/u_{\tau,NR}^4$ and $[\overline{\omega_i'\omega_i'}/2] \times \nu_u^2/u_{\tau,NR}^4$ with y^+ for the non-reacting case at $t/t_f = 3.99$. Experimental measurements of $\overline{\rho\tilde{\varepsilon}}/2\mu_u \times \nu_u^2/u_{\tau,NR}^4$ from Balint et al.[54] and DNS predictions of Gorski et al.[6] are also shown here along with the present DNS predictions.

obtained close to the wall (i.e., $y^+ < 30$). However, the contribution of $\overline{\omega_i}\,\overline{\omega_i}/2$ drops significantly away from the wall and $\overline{\omega_i'\omega_i'}/2$ becomes the dominant contributor to $\overline{\Omega}$ (i.e., $\overline{\Omega} \approx \overline{\omega_i'\omega_i'}/2$) for $y^+ > 30$.

Gorski et al.[6] presented the variations of the following fluctuating components of T_I based on their DNS data and compared them with respect to the experimental results by Balint et al.:[65]
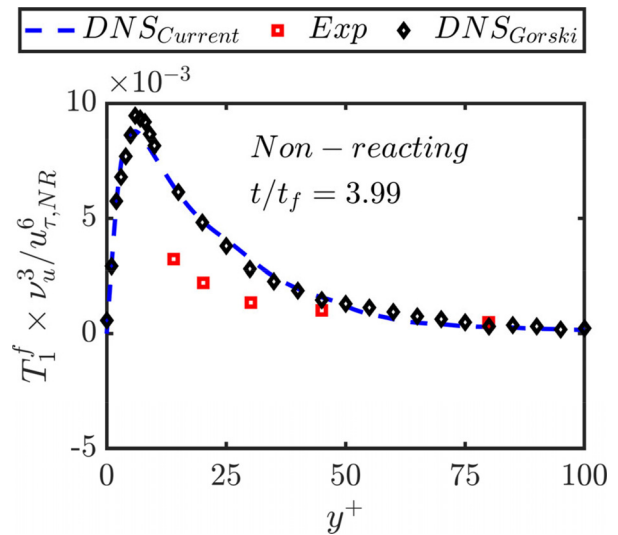

FIG. 21. Variations of $T_1^f \times \nu_u^3/u_{\tau,NR}^6$ with y^+ for the non-reacting case at $t/t_f = 3.99$.
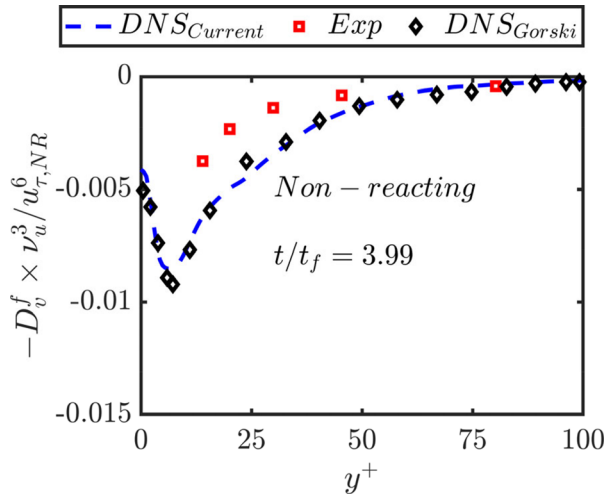
FIG. 22. Variations of the normalized $-D_v^f \times \nu_u^3 / u_{\tau,NR}^6$ with y^+ for the non-reacting case at $t/t_f = 3.99$.

$$T_1^f = \overline{\omega_i' \omega_k'} \frac{\partial \overline{u}_i}{\partial x_k} + \overline{\omega_i' \frac{\partial u_i'}{\partial x_k}} \overline{\omega}_k + \overline{\omega_i' \omega_k \frac{\partial u_i'}{\partial x_k}}, \quad (A1)$$

$$-D_v^f = -D_v + \nu \frac{\partial \widetilde{\omega}_i}{\partial x_j} \frac{\partial \widetilde{\omega}_i}{\partial x_j} = -\nu \overline{\frac{\partial \omega_i'}{\partial x_j} \frac{\partial \omega_i'}{\partial x_j}}. \quad (A2)$$

The variations of the terms $T_1^f \times \nu_u^3 / u_{\tau,NR}^6$ and $(-D_v^f) \times \nu_u^3 / u_{\tau,NR}^6$ with y^+ for the non-reacting case at $t/t_f = 3.99$ are presented in Figs. 21 and 22, respectively, along with the DNS results of Gorski *et al.*[6] and experimental measurements by Balint *et al.*[65] The present non-reacting flow results remain in good agreement with the DNS results of Gorski *et al.*[6] The qualitative agreement with experimental measurements by Balint *et al.*[65] remains satisfactory but some quantitative mismatch is not surprising because the reported experimental data[54] corresponds to $Re_\tau = 890$.

Moreover, the overprediction of the magnitudes of $T_1^f \times \nu_u^3 / u_{\tau,NR}^6$ and $(-D_v^f) \times \nu_u^3 / u_{\tau,NR}^6$ of the present non-reacting case in comparison to the experimental measurements by Balint *et al.*[65] is similar to the DNS results by Gorski *et al.*[6] It is worth noting that D_v^f was not directly measured by Balint *et al.*[65] The estimation of D_v^f was found as the residual of all the other directly measured terms in the balance equation. Therefore, it accumulates all the experimental errors, which thus may contribute to the quantitative disagreement between the DNS results and experimental estimations of D_v^f. Although the results for the non-reacting flow case at $t/t_f = 3.99$ are shown in Figs. 20–22, these variations remain qualitatively similar at other time instants considered in this paper, which are not here for the sake of brevity.

REFERENCES

[1] A. Perry and M. Chong, "A description of eddying motions and flow patterns using critical-point concepts," Annu. Rev. Fluid Mech. **19**, 125–155 (1987).

[2] M. Chong, A. Perry, and B. Cantwell, "A general classification of three-dimensional flow fields," Phys. Fluids **2**, 765–777 (1990).

[3] S. Corrsin, "Investigation of flow in an axially symmetrical heated jet of air," NACA Report No. W-94, 1943.

[4] P. A. Libby, "On the prediction of intermittent turbulent flows," J. Fluid Mech. **68**, 273–295 (1975).

[5] C. Dopazo and E. E. O'Brien, "Intermittency in free turbulent shear flows," in *Turbulent Shear Flows I*, edited by F. Durst, B. E. Launder, F. W. Schmidt, and J. H. Whitelaw (Springer, Berlin, Heidelberg, 1979).

[6] J. J. Gorski, J. M. Wallace, and P. M. Bernard, "The enstrophy equation budget of bounded turbulent shear flows," Phys. Fluids **6**, 3197 (1994).

[7] P. D. Belcher and R. D. Sandberg, "Variation of enstrophy production and strain rotation relation in a turbulent boundary layer," J. Fluid Mech. **812**, 321–348 (2017).

[8] P. E. Hamlington, A. Y. Poludnenko, and E. S. Oran, "Interactions between turbulence and flames in premixed reacting flows," Phys. Fluids **23**, 125111 (2011).

[9] N. Chakraborty, "Alignment of vorticity with strain rates in turbulent premixed flames," Eur. J. Mech. B **46**, 201–220 (2014).

[10] A. L. Lipatnikov, S. Nishiki, and T. Hasegawa, "A direct numerical simulation study of vorticity transformation in weakly turbulent premixed flames," Phys. Fluids **26**, 105104 (2014).

[11] N. Chakraborty, I. Konstantinou, and A. Lipatnikov, "Effects of Lewis number on vorticity and enstrophy transport in turbulent premixed flames," Phys. Fluids **28**, 015109 (2016).

[12] B. Bobbitt, S. Lapointe, and G. Blanquart, "Vorticity transformation in high Karlovitz number premixed flames," Phys. Fluids **28**, 015101 (2016).

[13] H. Wang, E. R. Hawkes, and J. H. Chen, "Turbulence-flame interactions in DNS of a laboratory high Karlovitz premixed turbulent jet flame," Phys. Fluids **28**, 095107 (2016).

[14] C. Dopazo, L. Cifuentes, and N. Chakraborty, "Vorticity budgets in premixed combusting turbulent flows at different Lewis numbers," Phys. Fluids **29**, 045106 (2017).

[15] N. Chakraborty, L. Wang, I. Konstantinou, and M. Klein, "Vorticity statistics based on velocity and density-weighted velocity in premixed reactive turbulence," J. Turbul. **18**, 825 (2017).

[16] V. Papapostolou, D. H. Wacks, M. Klein, N. Chakraborty, and H. G. Im, "Enstrophy transport conditional on local flow topologies in different regimes of premixed turbulent combustion," Sci. Rep. **7**, 11545 (2017).

[17] L. Cifuentes, A. M. Kempf, and C. Dopazo, "Local entrainment velocity in a premixed turbulent annular jet flame," Proc. Combust. Inst. **37**, 2493–2501 (2019).

[18] N. Chakraborty, M. Klein, and H. G. Im, "A comparison of entrainment velocity and displacement speed statistics in different regimes of turbulent premixed combustion," Proc. Combust. Inst. **38**, 2985–2992 (2021).

[19] A. Varma, U. Ahmed, and N. Chakraborty, "Effects of body forces on vorticity and enstrophy evolutions in turbulent premixed flames," Phys. Fluids **33**, 035102 (2021).

[20] R. Darragh, C. A. Z. Towery, M. A. Meehan, and P. E. Hamlington, "Lagrangian analysis of enstrophy dynamics in a highly turbulent premixed flame," Phys. Fluids **33**, 055120 (2021).

[21] C. J. Rising, A. J. Morales, M. K. Geikie, and K. A. Ahmed, "The effects of turbulence and pressure gradients on vorticity transport in premixed bluff-body flames," Phys. Fluids **33**, 017106 (2021).

[22] N. Chakraborty, "Influence of thermal expansion on fluid dynamics of turbulent premixed combustion and its modelling implications," Flow. Turbul. Combust. **106**, 753–806 (2021).

[23] A. J. Majda, "Vorticity, turbulence, and acoustics in fluid flow," SIAM Rev. **33**, 349–388 (1991).

[24] J. Jimenez, "Kinematic alignment effects in turbulent flows," Phys. Fluids A **4**, 652–654 (1992).

[25] A. Tsinober, E. Kit, and T. Dracos, "Experimental investigation of the field of velocity gradients in turbulent flows," J. Fluid Mech. **242**, 169–192 (1992).

[26] B. W. Zeff, D. Lanterman, D. R. McAllister, R. Roy, E. J. Kostelich, and D. P. Lathrop, "Measuring intense rotation and dissipation in turbulent flows," Nature **421**, 146–149 (2003).

[27] B. Lüthi, A. Tsinober, and W. Kinzelbach, "Lagrangian measurement of vorticity dynamics in turbulent flow," J. Fluid Mech. **528**, 87–118 (2005).

[28] P. E. Hamlington, J. Schumacher, and W. J. A. Dahm, "Local and nonlocal strain rate and vorticity alignment in turbulent flows," Phys. Rev. E **77**, 026303 (2008).

[29]H. Xu, A. Pumir, and E. Bodenschatz, "The pirouette effect in turbulent flows," Nat. Phys. **7**, 709–712 (2011).

[30]W. T. Ashurst, A. R. Kerstein, R. M. Kerr, and C. H. Gibson, "Alignment of vorticity and scalar gradient with strain rate in simulated Navier Stokes turbulence," Phys. Fluids **30**, 2343 (1987).

[31]K. K. Nomura and S. E. Elghobashi, "The structure of inhomogeneous turbulence in variable density nonpremixed flames," Theor. Comput. Fluid Dyn. **5**, 153–175 (1993).

[32]O. N. Boratov, S. E. Elghobashi, and R. Zhong, "On the alignment of strain, vorticity and scalar gradient in turbulent, buoyant, nonpremixed flames," Phys. Fluids **10**, 2260–2268 (1998).

[33]F. A. Jaberi, D. Livescu, and C. K. Madnia, "Characteristics of chemically reacting compressible homogeneous turbulence," Phys. Fluids **12**, 1189–1210 (2000).

[34]A. N. Lipatnikov, V. A. Sabelnikov, S. Nishiki, and T. Hasegawa, "Does flame-generated vorticity increase turbulent burning velocity?," Phys. Fluids **30**, 081702 (2018).

[35]A. M. Steinberg, J. F. Driscoll, and S. L. Ceccio, "Three-dimensional temporally resolved measurements of turbulence-flame interactions using orthogonal-plane cinema-stereoscopic PIV," Exp. Fluids **47**, 527 (2009).

[36]A. M. Steinberg, P. E. Hamlington, and X. Zhao, "Structure and dynamics of highly turbulent premixed combustion," Prog. Energy Combust. Sci. **85**, 100900 (2021).

[37]J. Lai, N. Chakraborty, and A. Lipatnikov, "Vorticity and enstrophy transport in head-on quenching of turbulent premixed flames," Eur. J. Mech. B **65**, 384–397 (2017).

[38]T. Ohta, Y. Onishi, and Y. Sakai, "Modulation of wall turbulence by propagating flame of premixed hydrogen–air combustion," Combust. Flame **241**, 112132 (2022).

[39]H. Tennekes and J. L. Lumley, *A First Course in Turbulence*, 1st ed. (MIT Press, Cambridge, Massachusetts, 1972).

[40]K. W. Jenkins and R. S. Cant, "Direct numerical simulation of turbulent flame kernels," in *Recent Advances in DNS and LES: Proceedings of the Second AFOSR Conference, Rutgers—The State University of New Jersey*, New Brunswick, USA, edited by D. Knight and L. Sakell (Kluwer, Dordrecht, 1999), pp. 191–202.

[41]A. A. Wray, "Minimal storage time advancement schemes for spectral methods," NASA Ames Research Center, California, Report No. MS 202 A-1, 1990.

[42]E. F. Tarrazo, A. L. Sánchez, A. Liñán, and F. A. Williams, "A simple one-step chemistry model for partially premixed hydrocarbon combustion," Combust. Flame **147**, 32–38 (2006).

[43]M. Champion, B. Deshaies, G. Joulin, and K. Kinoshita, "Spherical flame initiation: Theory versus experiment for lean propane–air mixtures," Combust. Flame **65**, 319–337 (1986).

[44]L. He, "Critical conditions for spherical flame initiation in mixtures with high Lewis numbers," Combust. Theory Model. **4**, 159–172 (2000).

[45]C. V. Espí and A. Liñán, "Fast non-diffusive ignition of a gaseous reacting mixture subject to a point energy source," Combust. Theory Model. **5**, 485–498 (2001).

[46]C. V. Espí and A. Liñán, "Thermal-diffusive ignition and flame initiation by a local energy source," Combust. Theory Model. **6**, 297–315 (2002).

[47]N. Peters, *Turbulent Combustion*, 1st ed. (Cambridge University Press, 2000), pp. 66–169.

[48]T. Poinsot, T. Echekki, and M. Mungal, "A study of the laminar flame tip and implications for turbulent premixed combustion," Combust. Sci. Technol. **81**, 45–73 (1992).

[49]T. M. Alshaalan and C. J. Rutland, "Wall heat flux in turbulent premixed reacting flow," Combust. Sci. Technol. **174**, 135–165 (2002).

[50]T. M. Alshaalan and C. J. Rutland, "Turbulence, scalar transport, and reaction rates in flame-wall interaction," Proc. Combust. Inst. **27**, 793–799 (1998).

[51]A. Gruber, R. Sankaran, E. R. Hawkes, and J. H. Chen, "Turbulent flame wall interaction: A direct numerical simulation study," J. Fluid Mech. **658**, 5–32 (2010).

[52]U. Ahmed, N. Chakraborty, and M. Klein, "Scalar gradient and strain rate statistics in oblique premixed flame-wall interaction within turbulent channel flows," Flow. Turbul. Combust. **106**, 701–732 (2021).

[53]U. Ahmed, N. Chakraborty, and M. Klein, "Assessment of Bray Moss Libby formulation for premixed flame-wall interaction within turbulent boundary layers: Influence of flow configuration," Combust. Flame **233**, 111575 (2021).

[54]J. Lai and N. Chakraborty, "Effects of Lewis number on head on quenching of turbulent premixed flames: A direct numerical simulation analysis," Flow. Turbul. Combust. **96**, 279–308 (2016).

[55]J. Sellmann, J. Lai, A. M. Kempf, and N. Chakraborty, "Flame surface density based modelling of head-on quenching of turbulent premixed flames," Proc. Combust. Inst. **36**, 1817–1825 (2017).

[56]U. Ahmed, N. A. K. Doan, J. Lai, M. Klein, N. Chakraborty, and N. Swaminathan, "Multiscale analysis of head-on quenching premixed turbulent flames," Phys. Fluids **30**, 105102 (2018).

[57]J. Lai, M. Klein, and N. Chakraborty, "Direct numerical simulation of head-on quenching of statistically planar turbulent premixed methane-air flames using a detailed chemical mechanism," Flow. Turbul. Combust. **101**, 1073–1091 (2018).

[58]J. Lai, U. Ahmed, M. Klein, and N. Chakraborty, "A comparison between head-on quenching of stoichiometric methane-air and hydrogen-air premixed flames using direct numerical simulations," Int. J. Heat Fluid Flow **93**, 108896 (2022).

[59]U. Ahmed, D. Apsley, T. Stallard, P. Stansby, and I. Afgan, "Turbulent length scales and budgets of Reynolds stress-transport for open-channel flows; friction Reynolds numbers $(Re_\tau) = 150$, 400 and 1020," J. Hydraul. Res. **59**, 36–50 (2021).

[60]C. S. Yoo and H. G. Im, "Characteristic boundary conditions for simulations of compressible reacting flows with multi-dimensional, viscous and reaction effects," Combust. Theor. Modell. **11**, 259–286 (2007).

[61]G. Bruneaux, K. Akselvoll, T. J. Poinsot, and J. H. Ferziger, "Flame-wall interaction simulation in a turbulent channel flow," Combust. Flame **107**, 27–36 (1996).

[62]G. Bruneaux, T. J. Poinsot, and J. H. Ferziger, "Premixed flame-wall interaction in a turbulent channel flow: Budget for the flame surface density evolution equation and modelling," J. Fluid Mech. **349**, 191–219 (1997).

[63]S. B. Pope, *Turbulent Flows*, 1st ed. (Cambridge University Press, Cambridge, 2000).

[64]D. C. Wilcox, *Turbulence Modeling for CFD*, 2nd ed. (DCW Industries, 1998).

[65]J. L. Balint, P. Vukoslavcevic, and J. M. Wallace, "The transport of enstrophy in a turbulent boundary layer," in *Near-Wall Turbulence, Zoran Zaric Memorial Conference 1988*, edited by S. J. Kline and N. H. Afgan (Hemisphere, Washington, 1990), p. 932.